Inverse expression of Ten3 and Lphn2 across the developing mouse brain reveals a global strategy for circuit assembly

URee Chon[1,2,3], Daniel T. Pederick[1,3,4]*, Jun Ho Song[1], Yanbo Zhang[1], Isabella Rana[1,5], Liqun Luo[1]*

[1]Department of Biology, Howard Hughes Medical Institute, Stanford University, Stanford, CA 94305, USA
[2]Neurosciences PhD Program, Stanford University, Stanford, CA 94305, USA
[3]These authors contributed equally to this study
[4]Present address: Department of Neuroscience, Johns Hopkins University School of Medicine, Baltimore, MD, USA
[5]Present address: Neuroscience PhD Program, Columbia University, New York, NY, USA
*Corresponding authors: dpederi1@jh.edu, lluo@stanford.edu

SUMMARY

Precise wiring of neural circuits requires molecular strategies that ensure accurate target selection across diverse brain regions. Here, we identify inverse expression between a ligand–receptor pair, Teneurin-3 (Ten3) and Latrophilin-2 (Lphn2), throughout the developing mouse brain. Ten3 and Lphn2 exhibit inverse expression gradients along a retinotopic axis orthogonal to the ephrin-A and EphA gradients; along the tonotopic axis across multiple brainstem auditory nuclei; and along the dorsomedial-ventrolateral axis in striatum and pallidum. Their inverse expression also creates discrete domains of cerebellar Purkinje cells and cerebellar nuclei along the mediolateral axis. Using conditional tag mice, we show that inverse Ten3 and Lphn2 expression patterns predict connectivity, following a 'Ten3→Ten3, Lphn2→Lphn2' rule in all above circuits. We further demonstrate a functional role for Lphn2 in executing this rule in Purkinje cells→cerebellar nuclei projection. Our findings reveal a global strategy of coordinating gene expression of key wiring molecules with circuit connectivity across the developing brain.

INTRODUCTION

Precise wiring of neural circuits during development is essential for proper information processing and behavior. The specificity of neuronal connectivity emerges from cell–cell interactions that rely on the differential expression of cell surface proteins (CSPs) to distinguish neuronal identity and guide the correct selection of synaptic partners.[1–5] However, while the human brain contains ~10^{11} neurons that form highly selective connections, the genome encodes only ~20,000 protein-coding genes, less than ~3,000 of which tile the cellular surface.[6,7] This disparity raises a fundamental question: how does the brain achieve such extraordinary wiring specificity with a limited molecular repertoire? Several mechanisms have been proposed to reconcile this disparity.[4] Graded expression enables different levels of the same CSP to specify different connections. Neurons may leverage combinatorial expression of multiple CSPs to generate unique molecular signatures. Additionally, alternative splicing and post-translational modifications can produce diverse isoforms from a single gene, expanding the functional repertoire of CSPs. However, one possible mechanism that has not been fully explored is the spatial and temporal reuse of CSPs across distinct anatomical regions and developmental stages to assemble diverse yet precise neural connections. For example, the ligand–receptor pair ephrin-A and EphA display inverse gradients of expression and use bidirectional heterophilic repulsion to instruct wiring specificity in the retina→superior colliculus projection in the visual system and the inferior olive→Purkinje cell projection in the cerebellum.[8–20] Despite extensive research on individual or pairs of CSPs that act as guidance molecules for circuit wiring, the spatial dynamics of a ligand–receptor pair at a whole brain scale, and how they cooperate to establish precise wiring of multiple circuits across development have not yet been systematically examined.

Teneurin-3 (Ten3) is an evolutionarily conserved type II transmembrane protein that instructs synaptic partner matching by homophilic adhesion.[21–23] We previously showed that Ten3 and the adhesion G protein-coupled-receptor latrophilin-2 (Lphn2) display inverse expression in two parallel hippocampal networks.[24] Ten3$^+$ proximal CA1 axons connect with Ten3$^+$ target neurons in the distal subiculum, and Lphn2$^+$ distal CA1 axons connect with Lphn2$^+$ target neurons in the proximal subiculum, following a 'Ten3→Ten3, Lphn2→Lphn2' rule relating CSP expression to connectivity. Ten3 and Lphn2 cooperate for target selection in the CA1→subiculum projection through Ten3–Ten3 homophilic attraction and Ten3–Lphn2 heterophilic repulsion.[24,25] In a companion manuscript, we further demonstrate that Ten3 and Lphn2 are repeatedly used to implement this connectivity rule and to establish wiring specificity across multiple nodes of the extended hippocampal network.[26]

Here, we reveal that inverse Ten3 and Lphn2 expression is not restricted to the hippocampal network but instead is present in many regions across the developing mouse brain, forming spatially stereotyped, inverse expression domains. We highlight four anatomically and functionally distinct systems: the visual system, auditory system, basal ganglia, and cerebellum. Across these regions, we observe that inverse Ten3 and Lphn2 expression patterns predict wiring specificity, following the 'Ten3→Ten3, Lphn2→Lphn2' connectivity rule. In the visual system, Ten3–Lphn2 inverse expression defines retinotopy along the dorsal-ventral axis orthogonal to the anterior-posterior axis defined by inverse ephrin-A–EphA expression.[15,18,19,27] In the auditory system, Ten3–Lphn2 inverse expression aligns with tonotopy across multiple brainstem auditory nuclei, providing a logic for how these circuits retain their exquisite wiring specificity across multiple synapses. In the basal ganglia, Ten3–Lphn2 inverse expression coincides with striatal-pallidal and cortical-striatal projections. In the cerebellum, Ten3–Lphn2 inverse expression matches Purkinje cell→cerebellar nuclei projection specificity, and we further demonstrate that Lphn2 is required for implementing the 'Ten3→Ten3' connectivity rule. These findings establish Ten3 and Lphn2 as components of a conserved molecular module that organizes specific and precise connectivity across anatomically and functionally distinct brain regions, uncovering a global principle for circuit organization throughout the developing brain.

RESULTS AND DISCUSSION

Ten3 and Lphn2 exhibit inverse expression across many regions of the developing brain

Given the inverse Ten3 and Lphn2 expression in the extended hippocampus network,[24,26] we first asked whether similar patterns extend to other regions of the brain during development. To address this, we characterized Ten3 and Lphn2 protein expression by fusing an HA-epitope tag to Ten3 and fluorescent mVenus to Lphn2[28], and characterized their distribution across the entire developing brain at multiple timepoints: embryonic day (E) 15 and 17, and postnatal day (P) 0, 2, 4, and 8. Brains were immunostained for Ten3^{HA} and Lphn2^{mV} using anti-HA and anti-GFP antibodies, respectively, and subsequently cleared using a modified version of iDISCO[29,30] and imaged with light-sheet microscopy (Figure 1A).

Across development, we observed Ten3 and Lphn2 expression in broad, largely non-overlapping and often adjacent regions spanning the forebrain, midbrain, hindbrain, and cerebellum (Figure 1B; Videos S1, 2). For example, at E17, we observed differential expression in discrete brain regions, including the striatum, hypothalamus, superior colliculus, nucleus sagulum, parabigeminal nucleus, cerebellar cortex, cochlear nucleus, spinal nucleus of the trigeminal, and nucleus of the solitary tract throughout coronal (Figure 1C), horizontal (Figure 1D), and sagittal (Figure 1E) sections. Ten3 was enriched medially and Lphn2 laterally in the superior colliculus (Figure 1C_2, D_5, E_{10}, E_{11}, white arrows). Conversely, Lphn2 was enriched medially and Ten3 laterally in multiple nuclei of the superior olivary complex (C_3, magenta arrow), as well as the mammillary body of the hypothalamus (D_8, orange arrow). In the cochlear nucleus (C_3, green arrow) and spinal trigeminal nucleus (C_4, yellow arrow), Lphn2 expression was higher in dorsal and Ten3 higher in ventral regions. Ten3 and Lphn2 also exhibited inverse expression in discrete nuclei of the thalamus (D_7, red arrow). In the cortex, Ten3 was high posteriorly whereas Lphn2 was high anteriorly (E_9, purple arrow); at a coronal section midway along the anterior–posterior axis, Lphn2 was high at lateral and medial edges whereas Ten3 was high in the intermediate zone (C_1, purple arrow). To facilitate the identification of anatomical regions that express Ten3 and Lphn2 throughout the

entire brain and across different timepoints, we developed an interactive, ImageJ-based visualization tool that enables users to actively navigate and examine anatomical regions of interest (Supplemental Data 1).

Together, these data show that Ten3 and Lphn2 proteins exhibit spatially segregated and largely inverse expression patterns throughout the developing brain. These inverse expression patterns do not generally follow a specific body axis but rather are specialized in each brain region. We decided to focus further investigation on four systems that exhibited robust and stereotyped Ten3–Lphn2 inverse expression: the visual system, auditory system, basal ganglia, and cerebellum, in the context of development and connectivity patterns of each system.

Ten3 and Lphn2 exhibit distinct temporal expression profiles across the developing brain

Our whole brain staining revealed that Ten3 and Lphn2 expression patterns change across developmental stages (Figure 1B). To quantify temporal dynamics of Ten3 and Lphn2 protein expression levels in the four systems, we performed immunostaining on coronal sections of *Ten3*$^{HA/HA}$*;Lphn2*$^{mV/mV}$ brains from E15 to P8. We processed samples across different stages together using identical staining and imaging conditions, such that their levels could be directly compared.

Visual information is transmitted from the retina to subcortical targets via retinal ganglion cell (RGC), whose axons form precise spatial maps in the superior colliculus (SC) and the lateral geniculate nucleus.[4] The SC is a midbrain structure where visual information is processed and integrated to coordinate motor behaviors, including eye and head movements, and orient attention to salient stimuli[31–37]. The SC receives input from RGCs in the retina during embryogenesis, where initial axonal outgrowth into the optic tract is observed by E12, followed by innervation of SC at E15.[27,38] Axon density within SC increases until birth, followed by axonal refinement.[27,38] Consistent with this early innervation, we observed robust inverse expression of Ten3 and Lphn2 in the SC throughout development, peaking during embryogenesis at E15 or earlier (Figure 2A). Expression levels of both Ten3 and Lphn2 continued to decline after birth, corresponding with the onset of activity-dependent refinement by cholinergic retinal waves.[39–41] We observed a stable inverse expression pattern throughout development, with Ten3 enriched in the medial SC and Lphn2 preferentially expressed in the lateral SC.

In the auditory system, sound information is detected at the cochlea and propagated to the brain via the auditory nerve, which connects the cochlea to the cochlear nucleus in the brainstem.[42–45] The cochlear nucleus sends bilateral connections to the nuclei of the superior olivary complex (SOC) in the brainstem, where signals from the left and right ears are integrated.[45–49] Neurons in the cochlear nucleus are born at E10.5–12.5 (anteroventral cochlear nucleus has a dorsal-ventral neuronal birth order gradient), and neurons of the SOC are born around E9–14 in a medio-lateral gradient.[50–52] The connectivity between the cochlear nucleus and the SOC is established during embryogenesis, where initial axon outgrowth toward the midline is observed at around E13, and topographic axonal connectivity starts to be established at E15.5.[53–55] During development, we observed Ten3 and Lphn2 inverse expression in all auditory brainstem nuclei. In the cochlear nucleus, peak expression levels of both Ten3 and Lphn2 were observed during embryogenesis at E17 or earlier, with a dramatic decrease in expression after P4 (Figure 2B). Interestingly, the peak expression of Ten3 and Lphn2 in the SOC was at around birth with a sharp reduction at P4 (Figure 2C). These expression profiles align with the known developmental timeline of the auditory brainstem. During embryogenesis, peak expression in the cochlear coincides with the period of axonal outgrowth from cochlear nucleus neurons. This is followed by peak expression at the target, the SOC, at P0, when axons mature into a calyx in the medial nucleus of the trapezoid body (MNTB)[56] and prune in the lateral superior olive (LSO), nuclei of the SOC. Expression declined by P4, a time when spontaneous cochlear activity begins to drive further synaptic refinement in the cochlear nucleus and the SOC.[57–60] Throughout development, Ten3 and Lphn2 maintained spatially inverse expression patterns in both the cochlear nucleus and the SOC.

The caudate putamen (CP, also referred to as dorsal striatum) of the basal ganglia is an important hub for integration of information for various functions including motor control, cognition, and emotion.[61–64] The spiny projection neurons constituting 95% of the CP neurons are born in a ventrolateral (E14-18) to dorsomedial (E18-P0) gradient throughout the entire CP.[65] Strikingly, we observed that Ten3 is highly enriched in the dorsomedial CP, whereas Lphn2 is predominantly expressed in the ventrolateral CP, with highest expression of Lphn2 at E15 and Ten3 at P0 (Figure 2D). Thus, the peak expression of Lphn2 and Ten3 coincided with the timing of neuronal birth in each region of CP. Earlier in development, the intermediate zone where Ten3 and Lphn2 domains

converged appeared relatively homogeneous. By P0, these regions resolved into discrete Ten3- and Lphn2-enriched clusters, forming spatially refined hotspots. This transition paralleled the onset of glutamatergic synapse innervation from both the thalamus[66] and cortex,[67,68] the maturation of synaptic connections, and dendritic spine growth in spiny projection neurons, during which bundles of corticostriatal axonal fibers begin to invade and penetrate the CP.

With more than 50% of the total number of neurons in CNS[69], the cerebellum is crucial for motor coordination, balance, posture,[70,71] as well as other non-motor functions, such as cognition, emotion, and reward processing.[72–75] The cerebellum comprises two separate parts—the cerebellar cortex and the cerebellar nuclei. The architecture of the cerebellar cortex is organized around Purkinje cells (PCs), which are GABAergic cells that form a single-cell layer between the granular and molecular layers, organizing and enhancing the lattice structure of the cerebellar cortex.[76,77] PCs are born around E11–13, following a lateral-to-medial order.[78–81] Climbing fibers from the inferior olive enter the cerebellar anlage and terminate at specific PC clusters that are grouped based on similar molecular identities at E15.[82–84] These PC clusters disperse into different lobules of the cerebellar cortex around E18, preceding postnatal lobulation.[83] Interestingly, we observed an inverse expression pattern of Ten3 and Lphn2 in both PCs and the cerebellar nuclei throughout development (Figure 2E). At E15, the cerebellar cortex and nuclei had not yet formed discernible structures; however, Ten3^{+} and Lphn2^{+} neurons were already largely segregated into distinct compartments (Figure S6B). By P0, Purkinje cells had begun organizing into a monolayer and neurons in the cerebellar nuclei into distinct clusters. As lobulation progressed postnatally, we observed the emergence of stable, inversely patterned expression across the cerebellar cortex and nuclei along the medial–lateral axis. Notably, the peak expression timepoint for Lphn2 preceded that of Ten3 (Figure 2E).

Together, these findings reveal that Ten3 and Lphn2 exhibit inverse expression that are both spatially segregated and temporally dynamic across multiple brain systems. Peak Ten3 and Lphn2 expression was observed during embryogenesis in the SC and cochlear nucleus, whereas expression in the SOC, striatum, and cerebellum peaked around birth (Figure 2F and G). In each system examined, the timeframe of peak protein expression coincided with the phase of axon targeting and synaptic maturation and refinement of each system. We next examined whether Ten3 and Lphn2 expression follows the 'Ten3→Ten3, Lphn2→Lphn2' connectivity rule and how this rule aligns with circuit properties in each system.

Ten3 and Lphn2 expression aligns with retinotopy along the dorsal–ventral axis of the retina

Retinotopy is a fundamental organization of the visual system—RGCs in nearby positions of the retina project axons to nearby target regions including the SC, such that the two-dimensional spatial map of the world in the retina is physically recapitulated in brain targets (Figure 3A). The orderly projection of RGC axons to the SC (equivalent of tectum in non-mammalian vertebrates) have been well described: RGCs from the anterior (nasal) retina project to posterior SC/tectum, posterior (temporal) retina to anterior SC/tectum, ventral retina to medial SC/tectum, and dorsal retina to lateral SC/tectum.[1,4] An extensive body of work has demonstrated that graded expression of cell-surface proteins ephrin-As and their receptors EphAs in both the retina and SC instructs retinotopic map along the anterior–posterior axis of the retina.[9,12,14,15,17] Much less is known about the mechanisms that control RGC axon targeting along the orthogonal dorsal–ventral axis, even though several candidates have been proposed, including ephrin-B and EphB, as well as Wnt signaling pathways. Ephrin-Bs and EphBs appear to play different roles in frogs and mice, and exhibit shallow expression gradients and produce mild phenotypes with *EphB* disruption;[85,86] Wnt signaling lacks loss-of-function evidence to support a direct instructive role.[87] Interestingly, *Ten3* mRNA has been reported to be expressed in the ventral retina and was shown to have defects in retinocollicular circuit wiring when deleted.[88] These findings suggested Ten3 as a candidate guidance molecule that may contribute to dorsal–ventral retinotopic organization.

Using immunostaining in a coronal section of *Ten3$^{HA/HA}$;Lphn2$^{mV/mV}$* mice at E15, we found that Ten3 was highly expressed in the ventral retina, whereas Lphn2 was highly expression in dorsal retina (Figure 3B). Quantification of normalized fluorescence intensity from flat-mount retina further revealed that Ten3 and Lphn2 proteins formed inverse gradients along the dorsal–ventral axis of the retina (Figure 3C, D). Three-dimensional reconstructions of cleared E15 whole brains visualized by light-sheet microscopy revealed that Ten3 and Lphn2 labeled discrete axon bundles in the optic tract, which comprises RGC axons connecting the eyes to brain targets

(Figure 3E). Higher magnification and cross section revealed two discrete Ten3^{+} bundles in the most anterior and posterior regions of the optic tract, along with a single Lphn2^{+} bundle in the middle. Inverse expression was also evident in the SC, with preferential expression of Ten3 in medial SC, inversely to Lphn2 enrichment in lateral SC (Figure 3F), forming opposing gradients (Figure 3G). Double *in situ* hybridization for *Ten3* and *Lphn2* mRNA confirmed local production of each CSP's mRNA in the SC (Figure S2A), suggesting that the presence of Ten3 and Lphn2 protein in SC is likely contributed by both RGC axons and SC target neurons. Notably, neither *Ten3* nor *Lphn2* expression was restricted to either excitatory or inhibitory neurons in the SC, as defined by *VGLUT2* and *VGAT*, respectively (Figure S2B, C). Given the known topographic projections of ventral and dorsal RGCs target medial and lateral SC,[1] and the established role of *Ten3* in retinocollicular organization,[88] our findings indicate that RGC axon projections follow the 'Ten3→Ten3, Lphn2→Lphn2' rule, and suggest that these proteins could participate in establishing the retinocollicular maps, perhaps in collaboration with other molecules.[85–87]

Ten3 and Lphn2 expression aligns with tonotopy in multiple brainstem nuclei along the ascending auditory pathway

Tonotopy is a fundamental organizing principle of the auditory system.[89] Sounds of different frequencies are represented by hair cells at different locations in the cochlea. Through ordered axonal projections, this tonotopic organization is recapitulated along the central auditory pathway in brainstem nuclei (Figure 4A) and beyond. These tonotopic maps are fundamental to frequency discrimination, pitch perception, and language processing.[90,91]

Immunostaining in *Ten3$^{HA/HA}$;Lphn2$^{mV/mV}$* mice at P0 revealed that Ten3 and Lphn2 proteins were distributed in opposing gradients in all cochlear nuclei, including the ventral cochlear nucleus (VCN; Figure 4B, C) as well as MNTB, superior paraolivary nucleus (SPN), and LSO in the SOC (Figure 4D, E). Strikingly, Ten3 expression always aligned with low-frequency regions, whereas Lphn2 with high-frequency regions (compare Figure 4B–E with Figure 4A). Double *in situ* hybridization for *Ten3* and *Lphn2* mRNA confirmed local production of Ten3 and Lphn2 in all nuclei of the auditory brainstem (Figure S3), suggesting that the protein expression is likely contributed by both input axons and target neurons. Given the known topographic projections between low- and high-frequency regions, these expression patterns indicate that the projections of auditory neurons between different nuclei follow the 'Ten3→Ten3, Lphn2→Lphn2' connectivity rule, and suggest that these proteins could participate in establishing tonotopic maps prior to the onset of hearing.

Analyzing Ten3 expression separately in axons and targets in the VCN→MNTB projections

We next aimed to dissect the contribution of Ten3 in axons and targets separately, using the VCN→MNTB projections as an example. To differentially label the same protein in axons and target, we generated conditional tag (*cTAG*) mice for Ten3 and Lphn2 (Figure S1). In *Ten3^{cTAG}* mice, Ten3 is tagged with an HA epitope tag, which is converted to a Halo-tag in the presence of Flp recombinase. Analogously, the *Lphn2^{cTAG}* mice labels Lphn2 with FLAG or SNAP in the absence or presence of Flp recombinase, respectively. Expression analysis in the hippocampus before and after introducing a germline-FlpO validated the fidelity of both tags, with Ten3^{HA} and Ten3^{Halo} expression in the proximal CA1 and dorsal subiculum, and Lphn2^{FLAG}/ Lphn2^{SNAP} expression localized to the distal CA1 and proximal subiculum (Figure S1). These expression patterns closely matched the endogenous Ten3 protein expression and Lphn2^{mV} expression previously reported.[23,24]

Projection neurons from the VCN to the MNTB are excitatory neurons that express *Slc17a6* encoding the vesicular glutamate transporter VGLUT2, whereas neurons in the MNTB are exclusively inhibitory.[92,93] To selectively label Ten3^{+} excitatory projection neurons, we crossed *Ten3^{cTAG}* mice with *Slc17a6-Flp*, which expresses Flp in all VGLUT2^{+} glutamatergic neurons, including those in the VCN (Figure S4B). This strategy enabled us to independently examine Ten3^{Halo} from VCN axons and Ten3^{HA} produced by local MNTB neurons at the MNTB (Figure 4F).

In control *Ten3^{cTAG}* mice lacking Flp expression, Ten3^{HA} (but no Ten3^{Halo}) was detected in the VCN, consistent with the absence of recombination. In *Slc17a6-Flp;Ten3^{cTAG}* mice, we observed robust recombination throughout VCN, with conversion to Ten3^{Halo} completely replacing Ten3^{HA} by P0 (Figure 4G). At the target MNTB, *Ten3^{cTAG}* mice displayed Ten3^{HA} signal but no Ten3^{Halo} signal, consistent with lack of recombinase activity

in axons and targets. By contrast, *Slc17a6-Flp;Ten3^{cTAG}* mice exhibited Ten3^{Halo} signal that overlapped with Ten3^{HA} expression in the lateral region of the MNTB. Thus, axons of Ten3^{Halo+} VCN excitatory neurons preferentially target to regions enriched for Ten3^{HA+} inhibitory neurons in the MNTB (Figure 4H).

Our data reveal that Ten3 is predominantly expressed in excitatory neurons in the VCN, as in *Slc17a6-Flp;Ten3^{cTAG}* mice, we did not detect any residual Ten3^{HA} signals (Figure 4G, right panels). Moreover, given the complete conversion of Ten3^{HA} to Ten3^{Halo} in VCN, Ten3^{HA} signals in the MNTB are not contributed by VCN axons and derive exclusively from local MNTB neurons. This allowed us to quantify the relative contribution of Ten3 proteins in axons and targets. Comparing Ten3^{HA} levels in the MNTB in *Ten3^{cTAG}* and *Slc17a6-Flp;Ten3^{cTAG}* mice suggests that the majority of Ten3 protein in the MNTB is contributed by target neurons (Figure 4I). Finally, while Ten3^{Halo+} VCN axons terminated at Ten3^{HA} region in the lateral MNTB, providing direct evidence supporting the 'Ten3→Ten3' targeting rule, these axons traversed Ten3-negative (and Lphn2-positive) regions in the medial MNTB to reach their destination (Figure 4H, middle row). This observation highlights the selectivity of VCN axon targeting and suggests that repulsion from Lphn2 may contribute to this selectivity, as previously described in the hippocampal network.[24,26]

Ten3 and Lphn2 display inverse expression in the basal ganglia

We next focused on the basal ganglia, a key regulator of motor output, action selection, and decision making. Given that one of the dominant input regions of the basal ganglia, the CP, expressed Ten3 and Lphn2 in opposing gradients (Figure 2D), we examined whether target regions of the CP also exhibit opposing Ten3 and Lphn2 expression. GABAergic spiny projection neurons in the CP form two projection pathways—a direct pathway projecting to the globus pallidus internal segment (GPi) and substantia nigra, and an indirect pathway that first projects to the globus pallidus external segment (GPe). These two pathways are coarsely thought to facilitate and inhibit movement, respectively.[94–96] With inverse expression of Ten3 and Lphn2 observed both in CP and GPe (Video S1, 2) , we focused our further analysis on the indirect (CP→GPe) pathway (Figure 5A).

Immunostaining of Ten3 and Lphn2 revealed preferential expression of Ten3 in dorsomedial CP and GPe globally, inversely to Lphn2 enrichment in ventrolateral CP and GPe (Figure 2D, 5B, and 5C). Unlike the continuous gradients at embryonic stages (Figure 2D), Ten3^{+} regions in the dorsomedial CP formed spatially clustered hotspots by P4, intermingled with cortical axon bundles (Figure 5B). Lphn2^{+} regions maintained a broader distribution of expression throughout the ventrolateral CP. Near the central region of CP where the global gradients meet, Lphn2^{+} regions also formed hotspots. Double *in situ* hybridization for *Ten3* and *Lphn2* mRNA revealed a similar inverse expression pattern—preferential *Ten3* expression in the dorsomedial regions and preferential *Lphn2* expression in the ventrolateral regions of CP and GPe at P4 (Figure S5A, B). These experiments validated that at least a part of the proteins we visualized in both CP and GPe were produced locally rather than exclusively contributed by incoming axons.

CP is histochemically organized into two compartments, known as striosomes (patches) and the matrix.[97] However, co-expression of Ten3 and Lphn2 with μ-opioid receptor (MOR) or calbindin, markers of striosomes and extrastriosomal matrix, respectively,[97,98] revealed no clear correspondence between their expression patterns (Figure S5C, D), indicating that the heterogeneity in Ten3 and Lphn2 expression is unrelated to striosomes and matrix.

Quantification across the dorsomedial–ventrolateral axis of CP and GPe revealed inverse gradients of expression (Figure 5D and F). This inverse pattern was confirmed by Spearman's correlation analysis across animals, which revealed significant negative correlations between Ten3 and Lphn2 expression in both CP ($\rho = -0.737$; ****$p < 0.0001$; Figure 5E) and GPe ($\rho = -0.763$; ****$p < 0.0001$; Figure 5G). Three-dimensional reconstructions of cleared whole brains visualized by light-sheet microscopy reinforced the consistent spatial segregation of Ten3 and Lphn2 in CP and GPe (Video S3). Thus, Ten3 and Lphn2 proteins exhibited inverse expression in both the origin and target regions of CP→GPe pathway during development.

Striatopallidal projections follow the Ten3→Ten3 rule

Given that CP and GPe are both globally patterned by differential expression of Ten3 and Lphn2, we next asked whether CP→GPe projections follows the 'Ten3→Ten3' rule. To examine this, we injected lentivirus expressing

FlpO-GFP into the CP of *Ten3*$^{cTAG/cTAG}$*;Lphn2*$^{mV/mV}$ mice at P0 and examined projection patterns of Ten3^{Halo+} CP axons in the GPe at P4 (Figure 5H). The robust Ten3^{Halo} signal confirmed local production of Ten3 in the CP. We found that Ten3^{Halo+} axons from the CP preferentially innervate the Ten3^{HA} regions of the GPe, while avoiding Lphn2^{mV} regions (Figure 5, I and J). Quantification of axon-target overlap confirmed substantial overlap of Ten3^{Halo+} CP axon signals within Ten3^{HA} target regions but little overlap in the Lphn2^{mV} target region (Figure 5K). Thus, CP→GPe projections follow the 'Ten3→Ten3' rule.

Corticostriatal projections follow the Ten3→Ten3 rule

Inputs to CP are known to play important roles in sensorimotor and cognitive functions,[61,62,99] and their implications in many pathophysiological disorders, including Huntington's and Parkinson's diseases, have been extensively studied.[100–102] CP receives input from across the cerebral cortex, as well as specific thalamic regions, mainly the parafascicular nuclei. We next examined whether input axons contribute to Ten3 expression in CP, and whether input projections also follow the 'Ten3→Ten3' rule. To do this we utilized our conditional tag allele in combination with cell-type-specific Flp drivers to differentially label Ten3 emanating from input axons versus the target arbors.

In the negative control mice without Flp recombinase expression, we observed no Ten3^{Halo} axon signal in the CP of *Ten3*^{cTAG} mice at P4 (Figure 6A). To visualize Ten3 production in CP neurons, which are predominantly GABAergic, we crossed *Ten3*^{cTAG} mice with *Slc32a1-Flp*, which expresses Flp in all GABAergic neurons (Figure S4A; note that none of the input neurons to CP are GABAergic). We observed robust Ten3^{Halo} signals in the CP (Figure 6B$_3$) in *Slc32a1-Flp mice*, confirming local production of Ten3 in the CP as indicated by our *in situ* analysis (Figure S5A). Interestingly, however, some of the Ten3^{Halo} signals overlapped with Ten3^{HA} signals of the CP (Figure 6B$_4$). The persistence of Ten3^{HA} is likely contributed by (1) expression of Ten3 in non-GABAergic CP neurons, such as cholinergic interneurons[103]; (2) incomplete recombination in GABAergic CP neurons; and/or (3) input axons from cortex and/or thalamus.

Next, we examined whether Ten3^{+} axons of thalamic excitatory neurons honed their projections to Ten3^{+} target regions of the CP. To test this, we crossed *Ten3*^{cTAG} mice with *Slc17a6-Flp*, which expresses Flp predominantly in thalamic excitatory neurons (Figure S4B). We did not detect Ten3^{Halo} axon labeling in the CP (Figure 6C), suggesting that thalamic Ten3^{+} axons do not innervate the CP at this developmental stage (P4). Indeed, we did not observe high levels of Ten3 protein expression in striatal-projecting thalamic nuclei during development including the parafascicular nuclei (Figure S5G). This contrasts with previous studies suggesting that Ten3 is expressed in both the CP and parafascicular nuclei, where it was proposed to regulate thalamo-striatal connectivity.[66,104] One possible explanation for this discrepancy is a divergence between *Ten3* mRNA and protein expression dynamics. Although prior studies have reported *Ten3* mRNAs in the parafascicular nuclei, we did not detect high levels of Ten3 protein in this region throughout development (Figure S5G). While *Ten3* mRNA persist in many brain regions into adulthood[105], Ten3 protein levels sharply decline after postnatal day 4, suggesting post-transcriptional regulation. The absence of detectable protein despite transcript expression could also reflect differential detecting thresholds.

Finally, to test whether Ten3^{+} cortical excitatory neurons project axons to CP, we crossed *Ten3*^{cTAG} mice with *Slc17a7-Flp*, where Flp is expressed primarily in cortical excitatory neurons but not any of the CP neurons (Figure S4C). Ten3^{Halo} signal was robustly detected in CP and coincided with Ten3^{HA}-expressing regions, including Ten3^{HA} hotspots at the intermediate zone between Ten3+ and Lphn2+ regions (Figure 6D). These data indicate that at least some Ten3^{+} cortical neurons project to CP, and such projections follow the 'Ten3→Ten3' rule. Interestingly, retrosplenial area and posterior parietal association areas of the cortex had high Ten3 expression (Supplemental Data 1) and are known to project to the dorsomedial CP.[106] These findings indicate that Ten3 expression may organize topographic cortical inputs to distinct CP subregions.

Together, the inverse expression patterns of Ten3 and Lphn2 at CP, both as global gradients and segregated hotspots at the intermediate zone, could be used to organize cortical input and pallidal output of CP neurons following the 'Ten3→Ten3' connectivity rule.

Ten3 and Lphn2 display inverse expression in both cerebellar Purkinje cells and cerebellar nuclei

The cerebellum is organized into a highly stereotyped architecture in which Purkinje cells (PCs) project topographically onto distinct domains of the cerebellar nuclei (CN) to regulate motor coordination, sensorimotor integration, and cognitive functions.[70–75] These projections are established early in development and exhibit precise spatial organization, yet the molecular mechanisms that guide PC axons to their appropriate nuclear targets remain poorly defined.

Given the structured topography of cerebellar cortico-nuclear projections, we asked whether Ten3 and Lphn2 participate in organizing connectivity between PCs and the CN. In coronal sections of P4 mouse brains, Ten3 and Lphn2 proteins were inversely expressed in PCs in alternating segments across the medial–lateral axis (Figure 7A). Higher magnification revealed sharp transitions in expression within the PC layer (Figure 7B). Quantification of normalized fluorescence intensities in the PC layer (Figure 7A) validated the reciprocity of Ten3 and Lphn2 across hemispheres in an individual mouse (Figure 7C). Spearman's correlation analysis confirmed an inverse relationship across difference mice ($\rho = -0.50$; ****$p < 0.0001$; Figure 7D). Inverse expression was also evident in the CN (Figure 7E), with preferential expression of Ten3 in dorsomedial and ventrolateral CN, inversely to Lphn2 enrichment in intermediate CN in this coronal section (Figure 7F). This pattern was confirmed by Spearman's correlation analysis across multiple mice ($\rho = -0.838$; ****$p < 0.0001$; Figure 7G). Double *in situ* hybridization for *Ten3* and *Lphn2* mRNA revealed similar inverse expression pattern throughout development in both PC layer and CN, validating that at least some of the protein expression in both PC and CN is contributed by local neurons (Figure S6A). Notably, *Ten3* and *Lphn2* expression in the CN did not conform to the anatomical boundaries of the medial, interposed, and dentate nuclei of CN, suggesting their expression is not restricted to specific anatomical CN subdivisions but instead reveals a new organizational principle. Furthermore, *Ten3* and *Lphn2* expression did not exclusively overlap with either excitatory marker VGLUT2 or the inhibitory marker VGAT, indicating that both *Ten3* and *Lphn2* may be expressed across diverse neuronal subtypes (Figure S6C, D).

Previous studies of the cerebellar cortex have divided PCs into transverse zones along the medial–lateral axis based on expression patterns of specific genes.[82–84] Each zone is subdivided into alternating arrays of parasagittal zebrin II-positive (zebrin$^+$) and zebrin II-negative (zebrin$^-$) stripes that run vertically across the entire cerebellar cortex. These parasagittal stripes are known to be evolutionarily conserved and are used as the main molecular marker to visualize the organization pattern of PCs during development.[82,107,108] Interestingly, zebrin patterns undergo dynamic changes during postnatal development. In the early postnatal period, zebrin is expressed in a subset of PCs. Between P10 and P12, its expression expands to all PCs. As development progresses, the patterning becomes more complex with an increasing number of alternating stripes. Between P12 and P15, zebrin is selectively downregulated in the zebrin$^-$ population, leading to the establishment of mature stripe patterns by P15.[82] Conversely, Ten3 and Lphn2 expression is initiated early in development around E15 (Figure S6B). To investigate if the patterns of Ten3 or Lphn2 expression coincides with zebrin stripes, we co-stained Ten3 and Lphn2 with either zebrin$^+$ or zebrin$^-$ molecular markers (Figure S6E, F). When we examined the co-expression of Ten3 and Lphn2 with aldolase C or PlcB4, markers of zebrin- positive and negative markers, respectively,[109,110] we did not find correspondence in their expression patterns. Indeed, visualizing Ten3$^+$ and Lphn2$^+$ PCs in 3D revealed that many parasagittal stripes of Ten3 and Lphn2 apparent from sections (e.g., Figure 7A) were in fact connected in 3D, forming continuous patches (Figure 7H, Video S4). The continuous expression of Ten3 and Lphn2 in 3D could nevertheless be segmented into four separable domains per hemisphere. Notably, 3D analysis of expression in the CN also revealed four discrete domains spanning both the anterior–posterior and medial–lateral axes (Video S5). Across the CN, the four expression domains of Ten3 and Lphn2 partitioned the entire CN, rather than aligning strictly with individual anatomical nuclei, suggesting that Ten3 and Lphn2 may define a molecular organization distinct from the cytoarchitectural boundaries. The observed Ten3 and Lphn2 pattern in the PC layer stands in stark contrast to the column-like organization typically associated with parasagittal stripes across all axes (Video S6). This deviation from the canonical stripe-based architecture is striking, as most well-known cerebellar molecular markers conform to a highly repetitive and stripe-like pattern. The identification of only four broad, continuous domains challenges prevailing notions of cerebellar organization and reveals a new spatial organization of Purkinje cells. Together, our data indicates that inverse Ten3 and Lphn2 expression represent novel molecular heterogeneity, offering a different framework to molecularly define PC organization.

Furthermore, this unique inverse expression pattern may reflect previously unreported functional organization within the cerebellar circuits.

To assess the stereotypy of Ten3 and Lphn2 expression in the cerebellar cortex, we quantified spatial similarity using Dice similarity coefficient (DSC). DSC measures the accuracy of spatial overlap, where 0 represents complete spatial segregation, 0.5 approximates spatial randomness, and 1 represents complete spatial overlap. After signal segmentation using Illastik, comprehensive object segmentation using SAM2-based algorithm, and whole brain registration using elastix on P0 brains (see Experimental Procedures for detail), we compared intra-hemispheric, inter-hemispheric, and inter-animal overlap of Ten3 or Lphn2 in the entire cerebellar cortex. DSC analysis revealed minimal intra-hemispheric overlap between Ten3 and Lphn2—consistent with their inverse expression patterns, and high inter-hemispheric and inter-animal similarity for either Ten3 or for Lphn2—indicating robust spatial stereotypy (Figure 7I). Importantly, the degree of spatial stereotypy we observed in the cerebellar cortex was comparable to that seen in other regions with well-established, highly stereotyped expression patterns, such as the subiculum, mammillary body, and superior colliculus (Figure S6G).

Purkinje cell→cerebellar nuclei projections follow the 'Ten3→Ten3, Lphn2→Lphn2' rule

Given the inverse expression of Ten3 and Lphn2 in both PC and CN, we next tested whether the PC→CN projection follows the 'Ten3→Ten3, Lphn2→Lphn2' rule. To do this, we wanted to investigate whether Ten3^{+} axons of PCs overlapped with Ten3^{+} target region of CN. Specifically, we injected lentivirus expressing *FlpO-GFP* into the cerebellar cortex of *Ten3$^{cTAG/cTAG}$;Lphn2$^{mV/mV}$* mice at P0 and examined Ten3^{Halo} PC axons in the CN (Figure 7J). We found that Ten3^{Halo+} PC axons preferentially projected to the Ten3^{HA} regions of the CN and avoided Lphn2^{mV} regions of the CN (Figure 7, K–P). Quantitative analysis confirmed significantly greater overlap between Ten3^{Halo} axon signals with Ten3^{HA} target regions compared to Lphn2^{mV} target regions (Figure 7Q).

To test whether Lphn2^{+} Purkinje cells project to Lphn2^{+} regions of the CN, we injected the same lentivirus into the cerebellar cortex of *Ten3$^{cTAG/cTAG}$;Lphn2$^{cTAG/cTAG}$* mice at P0. This would switch Lphn2 expression from Lphn2^{FLAG} to Lphn2^{SNAP} in PC axons, while leaving Ten3^{HA} unrecombined in CN target region (Figure 7R). Indeed, Lphn2^{SNAP+} PC axons projected preferentially to Ten3^{-} regions of the CN, avoiding Ten3^{HA} territories (Figure 7S–X), and quantitative analysis confirmed this preference (Figure 7Y).

In summary, Ten3 and Lphn2 show an inverse expression pattern in both the PCs and CN, and PC→CN projections follow the 'Ten3→Ten3, Lphn2→Lphn2' rule. Together with our findings in the visual, auditory, and basal ganglia systems (Figures 3–6), as well as the extended hippocampal network,[24,26] these findings reveal a generalizable mechanism by which spatially segregated Ten3 and Lphn2 could guide the formation of precise long-range connections in parallel networks using the 'Ten3→Ten3, Lphn2→Lphn2' rule.

Lphn2 is required for targeting precision of PC→CN axons

Finally, we asked whether Lphn2 plays a functional role in executing the 'Ten3→Ten3' projection rule observed in the cerebellum, similar to what we have shown in the extended hippocampal network.[24,26] Due to the complex nature of Ten3 connectivity in the cerebellum, traditional tracing approaches were not feasible, as Flp-driver lines that selectively target PCs during the embryonic window when Ten3 and Lphn2 expression begins were unavailable. Therefore, we used our conditional tag mice to examine if Ten3^{+} axons of PCs mistargeted to Ten3^{-} regions of CN when *Lphn2* was deleted. We injected *LV-FlpO-GFP* into PCs of *En1-Cre;Lphn2$^{+/+}$;Ten3^{cTAG}* mice (control, Figure 8A) or *En1-Cre;Lphn2$^{fl/fl}$;Ten3^{cTAG}* mice (experimental, Figure 8B) at P0. *En1*, encoding Engrailed homeobox 1, is expressed in developing rhombomere I that gives rise to both PCs and CN. Recombination in both regions was confirmed with a Cre-dependent reporter (Figure S4D), which will result in *Lphn2* being deleted in both PCs and CN. In line with previous results, Ten3^{Halo+} axons from PCs selectively targeted Ten3^{HA} regions in the anterior, intermediate, and posterior CN in *Lphn2$^{+/+}$* control mice (Figure 8, C–F). By contrast, Ten3^{Halo+} axons from PCs targeted more broadly into Ten3^{-} CN regions (non-Ten3^{HA} regions) in *Lphn2^{cKO}* mice, indicative of mistargeting (Figure 8, G–J, red arrows). This mistargeting was observed at all levels of the anterior–posterior axis. Despite the loss of targeting specificity, some Ten3^{Halo+} PC axons still innervated Ten3^{HA} domains of the CN, which could be contributed by Ten3–Ten3 homophilic attraction not affected by our experimental manipulation. Additionally, the order in which Ten3^{Halo+} axons encounter Ten3- or Lphn2-

expressing domains may influence their targeting—contact with Ten3^{+} regions of CN first may preferentially stabilize these projections, causing Ten3^{Halo+} axons innervation of Ten3^{HA} domains.[26] Quantification of axonal overlap revealed a significant reduction in Ten3^{Halo} alignment with Ten3^{HA} regions ($P < 0.01$) and a significant increase in Ten3^{Halo} overlap in Ten3^{-} CN regions ($P < 0.01$) in *Lphn2*$^{fl/fl}$ mice compared to *Lphn2*$^{+/+}$ control mice (Figure 8K). These results indicate that *Lphn2* is required for PC→CN projections to follow the 'Ten3→Ten3' rule: restricting Ten3^{+} PC axons to appropriate Ten3^{+} CN targets.

CONCLUDING REMARKS

In this study, we found striking, inverse expression of cell-surface proteins Ten3 and Lphn2 across the visual, auditory, basal ganglia, and cerebellar circuits during development. These inverse expression patterns emerge in three distinct modes: 1) gradients in the retina–superior colliculus of the visual circuit and the cochlear nucleus–superior olivary complex of the auditory circuit (Figure 3 and 4); 2) discrete domains in the cerebellum (Figure 6) and the extended hippocampus described elsewhere;[26] and 3) a combination of both in the striatal circuit (Figure 5). These distinct spatial expression modes may reflect different underlying organizational logics for specific circuits. In retinotopic and tonotopic maps, nearby neurons project to nearby targets to preserve continuous spatial and frequency maps. Continuous gradients of wiring molecules enable their levels to instruct targeting specificity.[1,15–20] By contrast, expression in discrete domains may serve as independent modules for circuit segregation and parallel information processing, as in the case of the medial and lateral subnetworks in the extended hippocampal circuit.[111] The global gradients of Ten3 and Lphn2 expression in CP may reflect continuous representation of sensorimotor function of the basal ganglia.[112,113] The discrete hotspots in CP and discrete domains in the cerebellum of Ten3 and Lphn2 expression we discovered do not match with previous described striosomes/matrix or parasagittal zebrin± bands, suggesting novel molecular organizations, the functional significance of which remains to be discovered.

The temporal dynamics of Ten3 and Lphn2 expression suggest a universal role in target selection. Across all systems examined, peak expression of these proteins coincides with the critical windows of axons selecting with which subregion within a specific target to make connections. Notably, in the auditory, striatal, and cerebellar circuits, Lphn2 expression correlated with earlier-born and Ten3 with later-born neurons, suggesting Ten3 and Lphn2 may establish connectivity across temporally distinct neuronal populations through sequential molecular expression. This exquisite spatiotemporal regulation of CSP expression allows a limited set of molecules to direct wiring of many circuits across diverse brain regions.

Interestingly, the inverse expression of Ten3 and Lphn2 is observed across a diverse array of brain regions, including the forebrain, midbrain, and hindbrain, despite their distinct developmental origins. This raises an intriguing question about whether a conserved regulatory mechanism governs this expression pattern across the brain, or if region-specific cues independently establish similar molecular expression patterns. Regardless of details of the regulatory mechanisms, our findings suggest that to accommodate the increasing complexity of the nervous system during evolution, it might be simpler to tweak expression patterns of key existing wiring molecules, than to reinventing new wiring molecules.

Together with our findings in the companion manuscript (Gingrich et al.), these results define a conserved molecular logic for target recognition that is used repeatedly across brain regions to establish precise neural circuits. The inverse expression of Ten3 and Lphn2 across multiple brain regions, along with their molecular function as a ligand–receptor pairs mediating both attraction and repulsion, reveals a global molecular strategy by which distinct circuits achieve precise circuit assembly throughout development.

Limitations of the study

While our study provides a foundational atlas of Ten3 and Lphn2 expression, several limitations remain. First, although we focused on four representative circuits, many other brain regions also exhibit inverse expression patterns of Ten3 and Lphn2. These regions may likewise employ the 'Ten3→Ten3, Lphn2→Lphn2' rule to guide circuit assembly, which need to be investigated in future studies. Second, in addition to regulating target selection

during development for the specific Ten3 and Lphn2 pair, there are other paralogs of teneurins (4 in total) and latrophilins (3 in total) in the mammalian genome that are implicated in synapse formation, organization and functional modulation.[114,115] However, unlike the striking inverse expression observed between Ten3 and Lphn2, most other teneurin and latrophilin paralogs display largely overlapping expression patterns.[115] Notably, several of these paralogs are also expressed in non-neuronal subpopulations, suggesting roles beyond classical neuron-neuron communication. Together, the broader expression across multiple cell types and overlapping expression patterns suggests that they may play broader roles, possibly contributing to synaptic function, including to ensure proper formation, stabilization, and long-term maintenance of synapses, in addition to spatially defined circuit assembly. Finally, although we described inverse expression of Ten3 and Lphn2 and the related connectivity rule in four systems, we only showed functional requirement of Lphn2 in the PC→CN connectivity. Future loss- and gain-of-function experiments will be required to demonstrate causal roles of Ten3 and Lphn2 in wiring the visual, auditory, and striatal systems. Given that Ten3 and Lphn2 are repeatedly used in the extended hippocampal network[24,26] and the PC→CN connectivity (Figure 8), it seems likely that Ten3 and Lphn2 will play an analogous role to instruct target selection in other circuits that follow the 'Ten3→Ten3, Lphn2→Lphn2' rule, perhaps in combination with other CSPs.

REFERENCES

1. Sperry, R.W. (1963). Chemoaffinity in the orderly growth of nerve fiber patterns and connections*. Proceedings of the National Academy of Sciences *50*, 703–710. https://doi.org/10.1073/pnas.50.4.703.

2. Kolodkin, A.L., and Tessier-Lavigne, M. (2011). Mechanisms and Molecules of Neuronal Wiring: A Primer. Cold Spring Harb Perspect Biol *3*, a001727. https://doi.org/10.1101/cshperspect.a001727.

3. Sanes, J.R., and Yamagata, M. (2009). Many Paths to Synaptic Specificity. Annu. Rev. Cell Dev. Biol. *25*, 161–195. https://doi.org/10.1146/annurev.cellbio.24.110707.175402.

4. Luo, L. (2020). Principles of Neurobiology (Garland Science).

5. Dickson, B.J. (2002). Molecular Mechanisms of Axon Guidance. Science *298*, 1959–1964. https://doi.org/10.1126/science.1072165.

6. The human brain - The Human Protein Atlas https://www.proteinatlas.org/humanproteome/brain.

7. Bausch-Fluck, D., Goldmann, U., Müller, S., van Oostrum, M., Müller, M., Schubert, O.T., and Wollscheid, B. (2018). The in silico human surfaceome. Proceedings of the National Academy of Sciences *115*, E10988–E10997. https://doi.org/10.1073/pnas.1808790115.

8. Cheng, H.-J., Nakamoto, M., Bergemann, A.D., and Flanagan, J.G. (1995). Complementary gradients in expression and binding of ELF-1 and Mek4 in development of the topographic retinotectal projection map. Cell *82*, 371–381. https://doi.org/10.1016/0092-8674(95)90426-3.

9. Drescher, U., Kremoser, C., Handwerker, C., Löschinger, J., Noda, M., and Bonhoeffer, F. (1995). In vitro guidance of retinal ganglion cell axons by RAGS, a 25 kDa tectal protein related to ligands for Eph receptor tyrosine kinases. Cell *82*, 359–370. https://doi.org/10.1016/0092-8674(95)90425-5.

10. Nakamoto, M., Cheng, H.-J., Friedman, G.C., McLaughlin, T., Hansen, M.J., Yoon, C.H., O'Leary, D.D.M., and Flanagan, J.G. (1996). Topographically Specific Effects of ELF-1 on Retinal Axon Guidance In Vitro and Retinal Axon Mapping In Vivo. Cell *86*, 755–766. https://doi.org/10.1016/S0092-8674(00)80150-6.

11. Frisén, J., Yates, P.A., McLaughlin, T., Friedman, G.C., O'Leary, D.D.M., and Barbacid, M. (1998). Ephrin-A5 (AL-1/RAGS) Is Essential for Proper Retinal Axon Guidance and Topographic Mapping in the Mammalian Visual System. Neuron *20*, 235–243. https://doi.org/10.1016/S0896-6273(00)80452-3.

12. Feldheim, D.A., Kim, Y.-I., Bergemann, A.D., Frisén, J., Barbacid, M., and Flanagan, J.G. (2000). Genetic Analysis of Ephrin-A2 and Ephrin-A5 Shows Their Requirement in Multiple Aspects of Retinocollicular Mapping. Neuron *25*, 563–574. https://doi.org/10.1016/S0896-6273(00)81060-0.

13. McLaughlin, T., Hindges, R., and O'Leary, D.D. (2003). Regulation of axial patterning of the retina and its topographic mapping in the brain. Current Opinion in Neurobiology *13*, 57–69. https://doi.org/10.1016/S0959-4388(03)00014-X.

14. Feldheim, D.A., Nakamoto, M., Osterfield, M., Gale, N.W., DeChiara, T.M., Rohatgi, R., Yancopoulos, G.D., and Flanagan, J.G. (2004). Loss-of-Function Analysis of EphA Receptors in Retinotectal Mapping. J. Neurosci. *24*, 2542–2550. https://doi.org/10.1523/JNEUROSCI.0239-03.2004.

15. Rashid, T., Upton, A.L., Blentic, A., Ciossek, T., Knöll, B., Thompson, I.D., and Drescher, U. (2005). Opposing Gradients of Ephrin-As and EphA7 in the Superior Colliculus Are Essential for Topographic Mapping in the Mammalian Visual System. Neuron *47*, 57–69. https://doi.org/10.1016/j.neuron.2005.05.030.

16. Egea, J., and Klein, R. (2007). Bidirectional Eph–ephrin signaling during axon guidance. Trends in Cell Biology *17*, 230–238. https://doi.org/10.1016/j.tcb.2007.03.004.

17. Suetterlin, P., and Drescher, U. (2014). Target-Independent EphrinA/EphA-Mediated Axon-Axon Repulsion as a Novel Element in Retinocollicular Mapping. Neuron *84*, 740–752. https://doi.org/10.1016/j.neuron.2014.09.023.

18. Lambot, M.-A., Depasse, F., Noel, J.-C., and Vanderhaeghen, P. (2005). Mapping Labels in the Human Developing Visual System and the Evolution of Binocular Vision. J. Neurosci. *25*, 7232–7237. https://doi.org/10.1523/JNEUROSCI.0802-05.2005.

19. Brown, A., Yates, P.A., Burrola, P., Ortuño, D., Vaidya, A., Jessell, T.M., Pfaff, S.L., O'Leary, D.D.M., and Lemke, G. (2000). Topographic Mapping from the Retina to the Midbrain Is Controlled by Relative but Not Absolute Levels of EphA Receptor Signaling. Cell *102*, 77–88. https://doi.org/10.1016/S0092-8674(00)00012-X.

20. Nishida, K., Flanagan, J.G., and Nakamoto, M. (2002). Domain-specific olivocerebellar projection regulated by the EphA-ephrin-A interaction. Development *129*, 5647–5658. https://doi.org/10.1242/dev.00162.

21. Hong, W., Mosca, T.J., and Luo, L. (2012). Teneurins Instruct Synaptic Partner Matching in an Olfactory Map. Nature *484*, 201–207. https://doi.org/10.1038/nature10926.

22. Mosca, T.J., Hong, W., Dani, V.S., Favaloro, V., and Luo, L. (2012). Trans-synaptic Teneurin signalling in neuromuscular synapse organization and target choice. Nature *484*, 237–241. https://doi.org/10.1038/nature10923.

23. Berns, D.S., DeNardo, L.A., Pederick, D.T., and Luo, L. (2018). Teneurin-3 controls topographic circuit assembly in the hippocampus. Nature *554*, 328–333. https://doi.org/10.1038/nature25463.

24. Pederick, D.T., Lui, J.H., Gingrich, E.C., Xu, C., Wagner, M.J., Liu, Y., He, Z., Quake, S.R., and Luo, L. (2021). Reciprocal repulsions instruct the precise assembly of parallel hippocampal networks. Science *372*, 1068–1073. https://doi.org/10.1126/science.abg1774.

25. Pederick, D.T., Perry-Hauser, N.A., Meng, H., He, Z., Javitch, J.A., and Luo, L. (2023). Context-dependent requirement of G protein coupling for Latrophilin-2 in target selection of hippocampal axons. eLife *12*, e83529. https://doi.org/10.7554/eLife.83529.

26. Gingrich, E.C., Pederick, D.T., Zhang, Y., and Luo, L. (2025). Ten3–Lphn2-mediated target selection across the extended hippocampal network demonstrates a repeated strategy for circuit assembly.

27. McLaughlin, T., and O'Leary, D.D.M. (2005). MOLECULAR GRADIENTS AND DEVELOPMENT OF RETINOTOPIC MAPS. Annual Review of Neuroscience *28*, 327–355. https://doi.org/10.1146/annurev.neuro.28.061604.135714.

28. Anderson, G.R., Maxeiner, S., Sando, R., Tsetsenis, T., Malenka, R.C., and Südhof, T.C. (2017). Postsynaptic adhesion GPCR latrophilin-2 mediates target recognition in entorhinal-hippocampal synapse assembly. Journal of Cell Biology *216*, 3831–3846. https://doi.org/10.1083/jcb.201703042.

29. Renier, N., Wu, Z., Simon, D.J., Yang, J., Ariel, P., and Tessier-Lavigne, M. (2014). iDISCO: A Simple, Rapid Method to Immunolabel Large Tissue Samples for Volume Imaging. Cell *159*, 896–910. https://doi.org/10.1016/j.cell.2014.10.010.

30. Chi, J., Crane, A., Wu, Z., and Cohen, P. (2018). Adipo-Clear: A Tissue Clearing Method for Three-Dimensional Imaging of Adipose Tissue. J Vis Exp, 58271. https://doi.org/10.3791/58271.

31. Sparks, D.L., Lee, C., and Rohrer, W.H. (1990). Population Coding of the Direction, Amplitude, and Velocity of Saccadic Eye Movements by Neurons in the Superior Colliculus. Cold Spring Harb Symp Quant Biol *55*, 805–811. https://doi.org/10.1101/SQB.1990.055.01.075.

32. Yilmaz, M., and Meister, M. (2013). Rapid Innate Defensive Responses of Mice to Looming Visual Stimuli. Current Biology *23*, 2011–2015. https://doi.org/10.1016/j.cub.2013.08.015.

33. Liang, F., Xiong, X.R., Zingg, B., Ji, X., Zhang, L.I., and Tao, H.W. (2015). Sensory Cortical Control of a Visually Induced Arrest Behavior via Corticotectal Projections. Neuron *86*, 755–767. https://doi.org/10.1016/j.neuron.2015.03.048.

34. Shang, C., Liu, Z., Chen, Z., Shi, Y., Wang, Q., Liu, S., Li, D., and Cao, P. (2015). A parvalbumin-positive excitatory visual pathway to trigger fear responses in mice. Science *348*, 1472–1477. https://doi.org/10.1126/science.aaa8694.

35. Wei, P., Liu, N., Zhang, Z., Liu, X., Tang, Y., He, X., Wu, B., Zhou, Z., Liu, Y., Li, J., et al. (2015). Processing of visually evoked innate fear by a non-canonical thalamic pathway. Nat Commun *6*, 6756. https://doi.org/10.1038/ncomms7756.

36. De Franceschi, G., Vivattanasarn, T., Saleem, A.B., and Solomon, S.G. (2016). Vision Guides Selection of Freeze or Flight Defense Strategies in Mice. Current Biology *26*, 2150–2154. https://doi.org/10.1016/j.cub.2016.06.006.

37. Ito, S., and Feldheim, D.A. (2018). The Mouse Superior Colliculus: An Emerging Model for Studying Circuit Formation and Function. Front Neural Circuits *12*, 10. https://doi.org/10.3389/fncir.2018.00010.

38. Osterhout, J.A., El-Danaf, R.N., Nguyen, P.L., and Huberman, A.D. (2014). Birthdate and Outgrowth Timing Predict Cellular Mechanisms of Axon Target Matching in the Developing Visual Pathway. Cell Reports *8*, 1006–1017. https://doi.org/10.1016/j.celrep.2014.06.063.

39. Feller, M.B., Wellis, D.P., Stellwagen, D., Werblin, F.S., and Shatz, C.J. (1996). Requirement for Cholinergic Synaptic Transmission in the Propagation of Spontaneous Retinal Waves. Science *272*, 1182–1187. https://doi.org/10.1126/science.272.5265.1182.

40. Stafford, B.K., Sher, A., Litke, A.M., and Feldheim, D.A. (2009). Spatial-Temporal Patterns of Retinal Waves Underlying Activity-Dependent Refinement of Retinofugal Projections. Neuron *64*, 200–212. https://doi.org/10.1016/j.neuron.2009.09.021.

41. Furman, M., Xu, H.-P., and Crair, M.C. (2013). Competition driven by retinal waves promotes morphological and functional synaptic development of neurons in the superior colliculus. J Neurophysiol *110*, 1441–1454. https://doi.org/10.1152/jn.01066.2012.

42. Willott, J.F. (2001). Handbook of Mouse Auditory Research: From Behavior to Molecular Biology (CRC Press).

43. Cant, N.B., and Benson, C.G. (2003). Parallel auditory pathways: projection patterns of the different neuronal populations in the dorsal and ventral cochlear nuclei. Brain Research Bulletin *60*, 457–474. https://doi.org/10.1016/S0361-9230(03)00050-9.

44. Di Bonito, M., and Studer, M. (2017). Cellular and Molecular Underpinnings of Neuronal Assembly in the Central Auditory System during Mouse Development. Front. Neural Circuits *11*. https://doi.org/10.3389/fncir.2017.00018.

45. Grothe, B., Pecka, M., and McAlpine, D. (2010). Mechanisms of Sound Localization in Mammals. Physiological Reviews *90*, 983–1012. https://doi.org/10.1152/physrev.00026.2009.

46. Webster, D.B., and Trune, D.R. (1982). Cochlear nuclear complex of mice. American Journal of Anatomy *163*, 103–130. https://doi.org/10.1002/aja.1001630202.

47. Hirsch, J.A., and Oertel, D. (1988). Synaptic connections in the dorsal cochlear nucleus of mice, in vitro. J Physiol *396*, 549–562. https://doi.org/10.1113/jphysiol.1988.sp016977.

48. Kandler, K., and Gillespie, D.C. (2005). Developmental refinement of inhibitory sound-localization circuits. Trends in Neurosciences *28*, 290–296. https://doi.org/10.1016/j.tins.2005.04.007.

49. Malmierca, M.S. (2015). Chapter 29 - Auditory System. In The Rat Nervous System (Fourth Edition), G. Paxinos, ed. (Academic Press), pp. 865–946. https://doi.org/10.1016/B978-0-12-374245-2.00029-2.

50. Pierce, E.T. (1973). Time of origin of neurons in the brain stem of the mouse. Prog Brain Res *40*, 53–65. https://doi.org/10.1016/S0079-6123(08)60679-2.

51. Marrs, G.S., Morgan, W.J., Howell, D.M., Spirou, G.A., and Mathers, P.H. (2013). Embryonic Origins of the Mouse Superior Olivary Complex. Dev Neurobiol *73*, 384–398. https://doi.org/10.1002/dneu.22069.

52. Shepard, A.R., Scheffel, J.L., and Yu, W.-M. (2019). Relationships between neuronal birthdates and tonotopic position in the mouse cochlear nucleus. J Comp Neurol *527*, 999–1011. https://doi.org/10.1002/cne.24575.

53. Marrs, G.S., and Spirou, G.A. (2012). Embryonic assembly of auditory circuits: spiral ganglion and brainstem. The Journal of Physiology *590*, 2391–2408. https://doi.org/10.1113/jphysiol.2011.226886.

54. Howell, D.M., Morgan, W.J., Jarjour, A.A., Spirou, G.A., Berrebi, A.S., Kennedy, T.E., and Mathers, P.H. (2007). Molecular guidance cues necessary for axon pathfinding from the ventral cochlear nucleus. J Comp Neurol *504*, 533–549. https://doi.org/10.1002/cne.21443.

55. Nakamura, P.A., and Cramer, K.S. (2011). Formation and Maturation of the Calyx of Held. Hear Res *276*, 70–78. https://doi.org/10.1016/j.heares.2010.11.004.

56. Hoffpauir, B.K., Kolson, D.R., Mathers, P.H., and Spirou, G.A. (2010). Maturation of synaptic partners: functional phenotype and synaptic organization tuned in synchrony. The Journal of Physiology *588*, 4365–4385. https://doi.org/10.1113/jphysiol.2010.198564.

57. Leake, P.A., Snyder, R.L., and Hradek, G.T. (2002). Postnatal refinement of auditory nerve projections to the cochlear nucleus in cats. Journal of Comparative Neurology *448*, 6–27. https://doi.org/10.1002/cne.10176.

58. Kim, G., and Kandler, K. (2003). Elimination and strengthening of glycinergic/GABAergic connections during tonotopic map formation. Nat Neurosci *6*, 282–290. https://doi.org/10.1038/nn1015.

59. Sanes, D.H., and Siverls, V. (1991). Development and specificity of inhibitory terminal arborizations in the central nervous system. Journal of Neurobiology *22*, 837–854. https://doi.org/10.1002/neu.480220805.

60. Kapfer, C., Seidl, A.H., Schweizer, H., and Grothe, B. (2002). Experience-dependent refinement of inhibitory inputs to auditory coincidence-detector neurons. Nat Neurosci *5*, 247–253. https://doi.org/10.1038/nn810.

61. Alexander, G.E., DeLong, M.R., and Strick, P.L. (1986). Parallel Organization of Functionally Segregated Circuits Linking Basal Ganglia and Cortex. Annual Review of Neuroscience *9*, 357–381. https://doi.org/10.1146/annurev.ne.09.030186.002041.

62. Parent, A., and Hazrati, L.-N. (1995). Functional anatomy of the basal ganglia. I. The cortico-basal ganglia-thalamo-cortical loop. Brain Research Reviews *20*, 91–127. https://doi.org/10.1016/0165-0173(94)00007-c.

63. Alheid, G.F., and Heimer, L. (1988). New perspectives in basal forebrain organization of special relevance for neuropsychiatric disorders: The striatopallidal, amygdaloid, and corticopetal components of substantia innominata. Neuroscience *27*, 1–39. https://doi.org/10.1016/0306-4522(88)90217-5.

64. Graybiel, A.M. (2005). The basal ganglia: learning new tricks and loving it. Current Opinion in Neurobiology *15*, 638–644. https://doi.org/10.1016/j.conb.2005.10.006.

65. Bayer, S.A., and Altman, J. (1987). Directions in neurogenetic gradients and patterns of anatomical connections in the telencephalon. Progress in Neurobiology *29*, 57–106. https://doi.org/10.1016/0301-0082(87)90015-3.

66. Tran, H., Sawatari, A., and Leamey, C.A. (2023). Ten-m3 plays a role in the formation of thalamostriatal projections. Developmental Neurobiology *83*, 255–267. https://doi.org/10.1002/dneu.22927.

67. Sohur, U.S., Padmanabhan, H.K., Kotchetkov, I.S., Menezes, J.R.L., and Macklis, J.D. (2014). Anatomic and Molecular Development of Corticostriatal Projection Neurons in Mice. Cerebral Cortex *24*, 293–303. https://doi.org/10.1093/cercor/bhs342.

68. Mesías, R.E., Zaki, Y., Guevara, C.A., Friedman, L.G., Hussein, A., Therrien, K., Magee, A.R., Tzavaras, N., Valle, P.D., Baxter, M.G., et al. (2023). Development of prefrontal corticostriatal connectivity in mice. Preprint at bioRxiv, https://doi.org/10.1101/2023.03.14.532475 https://doi.org/10.1101/2023.03.14.532475.

69. Wang, V.Y., and Zoghbi, H.Y. (2001). Genetic regulation of cerebellar development. Nat Rev Neurosci *2*, 484–491. https://doi.org/10.1038/35081558.

70. Paulin, M.G. (1993). The role of the cerebellum in motor control and perception. Brain, Behavior and Evolution *41*, 39–50. https://doi.org/10.1159/000113822.

71. Manto, M., Bower, J.M., Conforto, A.B., Delgado-García, J.M., da Guarda, S.N.F., Gerwig, M., Habas, C., Hagura, N., Ivry, R.B., Mariën, P., et al. (2012). Consensus Paper: Roles of the Cerebellum in Motor Control—The Diversity of Ideas on Cerebellar Involvement in Movement. Cerebellum *11*, 457–487. https://doi.org/10.1007/s12311-011-0331-9.

72. Klein, A.P., Ulmer, J.L., Quinet, S.A., Mathews, V., and Mark, L.P. (2016). Nonmotor Functions of the Cerebellum: An Introduction. AJNR Am J Neuroradiol *37*, 1005–1009. https://doi.org/10.3174/ajnr.a4720.

73. Sacchetti, B., Scelfo, B., and Strata, P. (2009). Cerebellum and emotional behavior. Neuroscience *162*, 756–762. https://doi.org/10.1016/j.neuroscience.2009.01.064.

74. Strata, P., Scelfo, B., and Sacchetti, B. (2011). Involvement of Cerebellum in Emotional Behavior. Physiol Res, S39–S48. https://doi.org/10.33549/physiolres.932169.

75. Mennink, L.M., van Dijk, J.M.C., and van Dijk, P. (2020). The cerebellar (para)flocculus: A review on its auditory function and a possible role in tinnitus. Hearing Research *398*, 108081. https://doi.org/10.1016/j.heares.2020.108081.

76. Braitenberg, V., and Atwood, R.P. (1958). Morphological observations on the cerebellar cortex. Journal of Comparative Neurology *109*, 1–33. https://doi.org/10.1002/cne.901090102.

77. Voogd, J., and Glickstein, M. (1998). The anatomy of the cerebellum. Trends in Neurosciences *21*, 370–375. https://doi.org/10.1016/S0166-2236(98)01318-6.

78. Inouye, M., and Murakami, U. (1980). Temporal and spatial patterns of Purkinje cell formation in the mouse cerebellum. Journal of Comparative Neurology *194*, 499–503. https://doi.org/10.1002/cne.901940302.

79. Hashimoto, M., and Mikoshiba, K. (2003). Mediolateral compartmentalization of the cerebellum is determined on the "birth date" of Purkinje cells. J Neurosci *23*, 11342–11351. https://doi.org/10.1523/JNEUROSCI.23-36-11342.2003.

80. Namba, K., Sugihara, I., and Hashimoto, M. (2011). Close correlation between the birth date of purkinje cells and the longitudinal compartmentalization of the mouse adult cerebellum. Journal of Comparative Neurology *519*, 2594–2614. https://doi.org/10.1002/cne.22640.

81. Beekhof, G.C., Osório, C., White, J.J., van Zoomeren, S., van der Stok, H., Xiong, B., Nettersheim, I.H., Mak, W.A., Runge, M., Fiocchi, F.R., et al. (2021). Differential spatiotemporal development of Purkinje cell populations and cerebellum-dependent sensorimotor behaviors. eLife *10*, e63668. https://doi.org/10.7554/eLife.63668.

82. Sillitoe, R.V., and Hawkes, R. (2013). Zones and Stripes: Development of Cerebellar Topography. In Handbook of the Cerebellum and Cerebellar Disorders (Springer, Dordrecht), pp. 43–59. https://doi.org/10.1007/978-94-007-1333-8_3.

83. Reeber, S.L., White, J.J., George-Jones, N.A., and Sillitoe, R.V. (2013). Architecture and development of olivocerebellar circuit topography. Front. Neural Circuits *6*. https://doi.org/10.3389/fncir.2012.00115.

84. White, J.J., and Sillitoe, R.V. (2013). Development of the cerebellum: from gene expression patterns to circuit maps. WIREs Developmental Biology *2*, 149–164. https://doi.org/10.1002/wdev.65.

85. Hindges, R., McLaughlin, T., Genoud, N., Henkemeyer, M., and O'Leary, D.D.M. (2002). EphB Forward Signaling Controls Directional Branch Extension and Arborization Required for Dorsal-Ventral Retinotopic Mapping. Neuron *35*, 475–487. https://doi.org/10.1016/S0896-6273(02)00799-7.

86. Mann, F., Ray, S., Harris, W.A., and Holt, C.E. (2002). Topographic Mapping in Dorsoventral Axis of the *Xenopus* Retinotectal System Depends on Signaling through Ephrin-B Ligands. Neuron *35*, 461–473. https://doi.org/10.1016/S0896-6273(02)00786-9.

87. Schmitt, A.M., Shi, J., Wolf, A.M., Lu, C.-C., King, L.A., and Zou, Y. (2006). Wnt–Ryk signalling mediates medial–lateral retinotectal topographic mapping. Nature *439*, 31–37. https://doi.org/10.1038/nature04334.

88. Dharmaratne, N., Glendining, K.A., Young, T.R., Tran, H., Sawatari, A., and Leamey, C.A. (2012). Ten-m3 Is Required for the Development of Topography in the Ipsilateral Retinocollicular Pathway. PLOS ONE *7*, e43083. https://doi.org/10.1371/journal.pone.0043083.

89. Kandler, K., Clause, A., and Noh, J. (2009). Tonotopic reorganization of developing auditory brainstem circuits. Nat Neurosci *12*, 711–717. https://doi.org/10.1038/nn.2332.

90. Oxenham, A.J., Bernstein, J.G.W., and Penagos, H. (2004). Correct tonotopic representation is necessary for complex pitch perception. Proc Natl Acad Sci U S A *101*, 1421–1425. https://doi.org/10.1073/pnas.0306958101.

91. Mengler, E.D., Hogben, J.H., Michie, P., and Bishop, D.V.M. (2005). Poor frequency discrimination is related to oral language disorder in children: a psychoacoustic study. Dyslexia *11*, 155–173. https://doi.org/10.1002/dys.302.

92. Ito, T., Bishop, D.C., and Oliver, D.L. (2011). Expression of glutamate and inhibitory amino acid vesicular transporters in the rodent auditory brainstem. Journal of Comparative Neurology *519*, 316–340. https://doi.org/10.1002/cne.22521.

93. Bonito, M.D., Narita, Y., Avallone, B., Sequino, L., Mancuso, M., Andolfi, G., Franzè, A.M., Puelles, L., Rijli, F.M., and Studer, M. (2013). Assembly of the Auditory Circuitry by a Hox Genetic Network in the Mouse Brainstem. PLOS Genetics *9*, e1003249. https://doi.org/10.1371/journal.pgen.1003249.

94. Lanciego, J.L., Luquin, N., and Obeso, J.A. (2012). Functional Neuroanatomy of the Basal Ganglia. Cold Spring Harb Perspect Med *2*, a009621. https://doi.org/10.1101/cshperspect.a009621.

95. Li, H., and Jin, X. (2023). Multiple dynamic interactions from basal ganglia direct and indirect pathways mediate action selection. eLife *12*, RP87644. https://doi.org/10.7554/eLife.87644.

96. Tanimura, Y., King, M.A., Williams, D.K., and Lewis, M.H. (2011). Development of repetitive behavior in a mouse model: Roles of indirect and striosomal basal ganglia pathways. Int J Dev Neurosci *29*, 461–467. https://doi.org/10.1016/j.ijdevneu.2011.02.004.

97. Brimblecombe, K.R., and Cragg, S.J. (2017). The Striosome and Matrix Compartments of the Striatum: A Path through the Labyrinth from Neurochemistry toward Function. ACS Chem. Neurosci. *8*, 235–242. https://doi.org/10.1021/acschemneuro.6b00333.

98. Tajima, K., and Fukuda, T. (2013). Region-specific diversity of striosomes in the mouse striatum revealed by the differential immunoreactivities for mu-opioid receptor, substance P, and enkephalin. Neuroscience *241*, 215–228. https://doi.org/10.1016/j.neuroscience.2013.03.012.

99. Tepper, J.M., Abercrombie, E.D., and Bolam, J.P. (2007). Basal ganglia macrocircuits. In Progress in Brain Research Gaba and the Basal Ganglia., J. M. Tepper, E. D. Abercrombie, and J. P. Bolam, eds. (Elsevier), pp. 3–7. https://doi.org/10.1016/S0079-6123(06)60001-0.

100. Milnerwood, A.J., and Raymond, L.A. (2007). Corticostriatal synaptic function in mouse models of Huntington's disease: early effects of huntingtin repeat length and protein load. J Physiol *585*, 817–831. https://doi.org/10.1113/jphysiol.2007.142448.

101. Bunner, K.D., and Rebec, G.V. (2016). Corticostriatal Dysfunction in Huntington's Disease: The Basics. Front. Hum. Neurosci. *10*. https://doi.org/10.3389/fnhum.2016.00317.

102. Martel, A.-C., and Galvan, A. (2022). Connectivity of the Corticostriatal and Thalamostriatal Systems in Normal and Parkinsonian States: An Update. Neurobiol Dis *174*, 105878. https://doi.org/10.1016/j.nbd.2022.105878.

103. Ahmed, N.Y., Knowles, R., and Dehorter, N. (2019). New Insights Into Cholinergic Neuron Diversity. Front. Mol. Neurosci. *12*. https://doi.org/10.3389/fnmol.2019.00204.

104. Tran, H., Sawatari, A., and Leamey, C.A. (2015). The glycoprotein Ten-m3 mediates topography and patterning of thalamostriatal projections from the parafascicular nucleus in mice. European Journal of Neuroscience *41*, 55–68. https://doi.org/10.1111/ejn.12767.

105. ISH Data :: Allen Brain Atlas: Mouse Brain https://mouse.brain-map.org/.

106. Hintiryan, H., Foster, N.N., Bowman, I., Bay, M., Song, M.Y., Gou, L., Yamashita, S., Bienkowski, M.S., Zingg, B., Zhu, M., et al. (2016). The mouse cortico-striatal projectome. Nat Neurosci *19*, 1100–1114. https://doi.org/10.1038/nn.4332.

107. Brochu, G., Maler, L., and Hawkes, R. (1990). Zebrin II: A polypeptide antigen expressed selectively by purkinje cells reveals compartments in rat and fish cerebellum. Journal of Comparative Neurology *291*, 538–552. https://doi.org/10.1002/cne.902910405.

108. Sillitoe, R.V., and Hawkes, R. (2002). Whole-mount Immunohistochemistry: A High-throughput Screen for Patterning Defects in the Mouse Cerebellum. J Histochem Cytochem. *50*, 235–244. https://doi.org/10.1177/002215540205000211.

109. Ahn, A.H., Dziennis, S., Hawkes, R., and Herrup, K. (1994). The cloning of zebrin II reveals its identity with aldolase C. Development *120*, 2081–2090. https://doi.org/10.1242/dev.120.8.2081.

110. Sarna, J.R., Marzban, H., Watanabe, M., and Hawkes, R. (2006). Complementary stripes of phospholipase Cβ3 and Cβ4 expression by Purkinje cell subsets in the mouse cerebellum. Journal of Comparative Neurology *496*, 303–313. https://doi.org/10.1002/cne.20912.

111. Moser, E.I., Kropff, E., and Moser, M.-B. (2008). Place cells, grid cells, and the brain's spatial representation system. Annu Rev Neurosci *31*, 69–89. https://doi.org/10.1146/annurev.neuro.31.061307.090723.

112. DeLong, M.R., and Georgopoulos, A.P. (1981). Motor Functions of the Basal Ganglia. In Comprehensive Physiology (John Wiley & Sons, Ltd), pp. 1017–1061. https://doi.org/10.1002/cphy.cp010221.

113. Foster, N.N., Barry, J., Korobkova, L., Garcia, L., Gao, L., Becerra, M., Sherafat, Y., Peng, B., Li, X., Choi, J.-H., et al. (2021). The mouse cortico–basal ganglia–thalamic network. Nature *598*, 188–194. https://doi.org/10.1038/s41586-021-03993-3.

114. Araç, D., and Li, J. (2019). Teneurins and latrophilins: two giants meet at the synapse. Current Opinion in Structural Biology *54*, 141–151. https://doi.org/10.1016/j.sbi.2019.01.028.

115. Liakath-Ali, K., Refaee, R., and Südhof, T.C. (2024). Cartography of teneurin and latrophilin expression reveals spatiotemporal axis heterogeneity in the mouse hippocampus during development. PLOS Biology *22*, e3002599. https://doi.org/10.1371/journal.pbio.3002599.

116. Kimmel, R.A., Turnbull, D.H., Blanquet, V., Wurst, W., Loomis, C.A., and Joyner, A.L. (2000). Two lineage boundaries coordinate vertebrate apical ectodermal ridge formation. Genes Dev. *14*, 1377–1389. https://doi.org/10.1101/gad.14.11.1377.

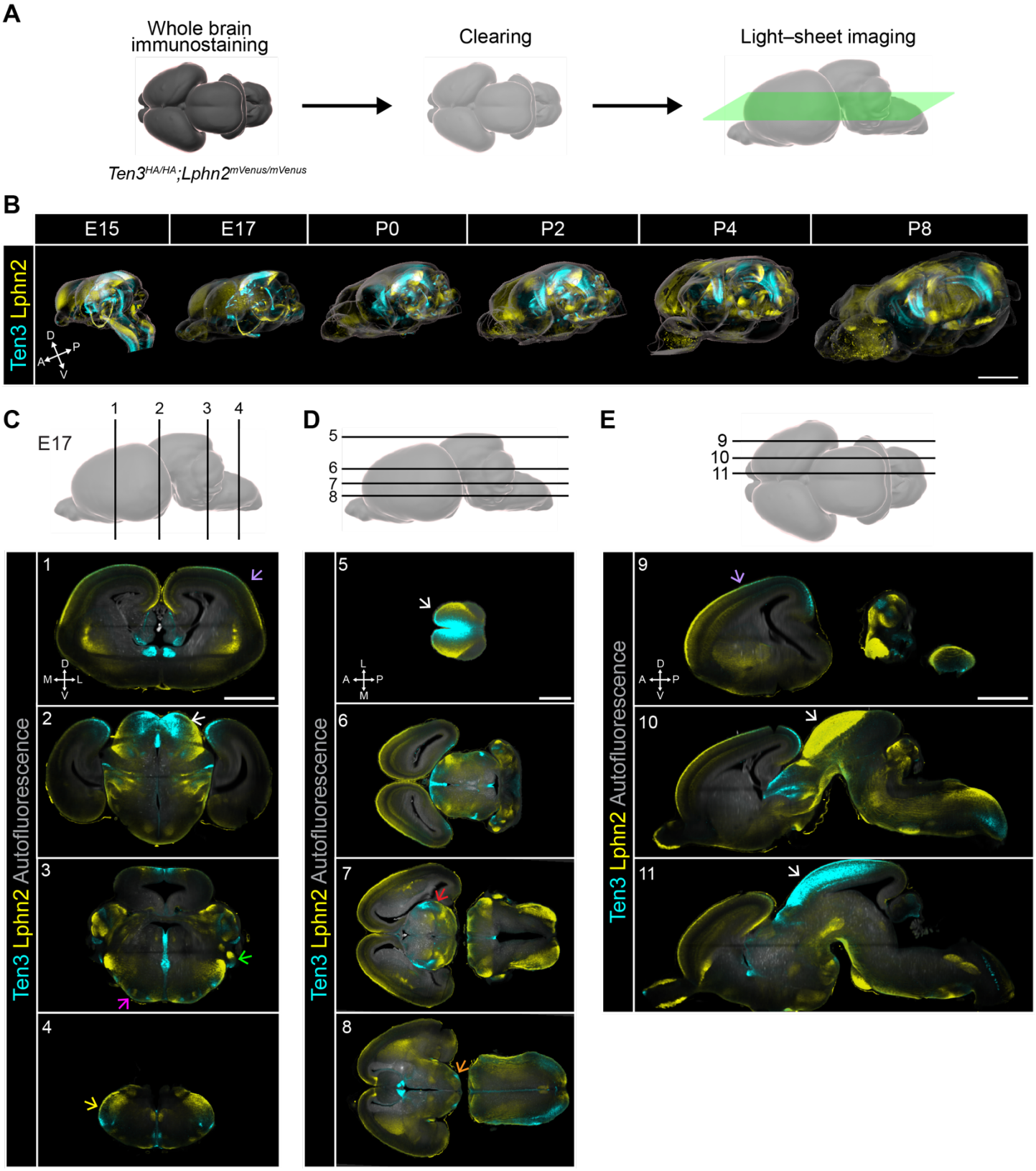

Figure 1. Whole brain staining of Ten3 and Lphn2 across development.
(A) Overview of the procedure used to stain whole mouse brains for Ten3 and Lphn2 proteins.
(B) 3D staining patterns of Ten3 and Lphn2 proteins in the mouse brain across different stages of development. E, embryonic day; P, postnatal day. Scale bar, 2 mm.
(C–E) Ten3 and Lphn2 protein expression in single optical sections in the coronal (C), horizontal (D), and sagittal (E) planes of the same 3D volume of an E17 brain imaged by light sheet microscopy. The number of

each image is matched with the section location (line) in the schematic above. Superior colliculus, white arrows; superior olivary complex, magenta arrow; ventral cochlear nucleus, green arrow; spinal trigeminal nucleus, yellow arrow; midbrain, red arrow; mammillary body of the hypothalamus, orange arrow; cortex, purple arrows. Detailed expression patterns in all brain regions of E17 and P2 mouse brains, including nucleus sagulum, parabigeminal nucleus, and nucleus of the solitary tract, can be found in Supplemental Data 1. Scale bars, 1 mm.

In this and all subsequent figures, A, anterior; P, posterior; D, dorsal; V, ventral; M, medial; L, lateral. Unless otherwise mentioned, all Ten3 and Lphn2 proteins were visualized with anti-HA and anti-GFP antibodies in *Ten3*$^{HA/HA}$;*Lphn2*$^{mV/mV}$ knock-in mice, respectively.

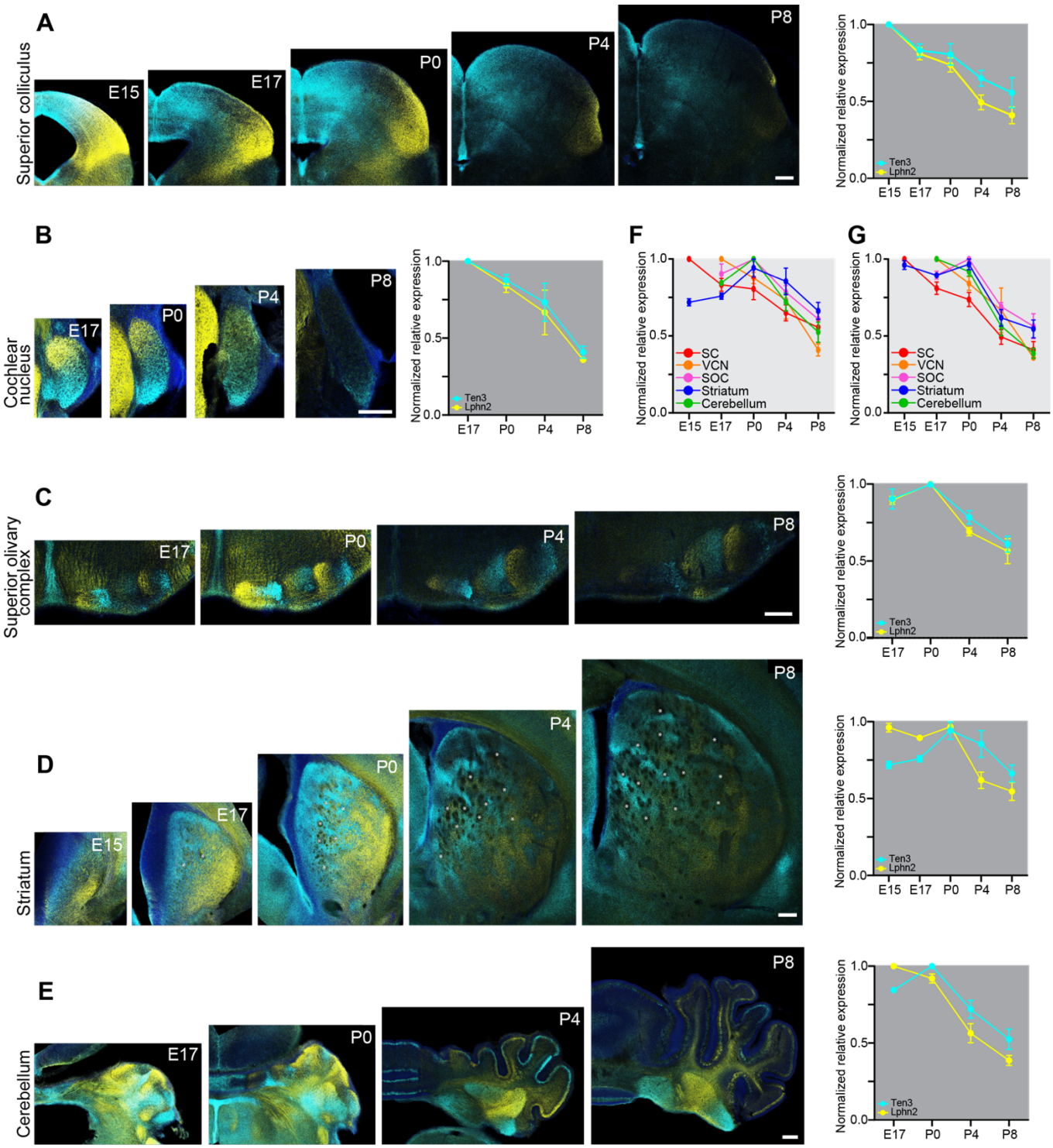

Figure 2. Ten3 and Lphn2 have different temporal expression patterns across brain regions.
(A–E) Coronal sections showing Ten3 and Lphn2 protein expression in the superior colliculus (A), ventral cochlear nucleus (B), superior olivery nucleus (C), caudate-putamen (D), and cerebellum (E) across multiple stages of development. Quantifications of normalized relative levels of expression are shown in the rightmost panels. * in P4 of panel D indicate cortical axon bundles passing through the striatum, creating "holes" in the Ten3 and Lphn2 expression patterns.
(F, G) Normalized relative Ten3 (F) and Lphn2 (G) protein expression in all areas throughout development. All sections were stained in the same batch of experiments under identical conditions and imaged under identical exposure settings to allow for comparative analysis of relative protein intensity across time. All quantification analysis done in n = 3 mice. Abbreviations: SC, superior colliculus; SOC, superior oliveary complex; VCN, ventral cochlear nucleus. Scale bar, 200 µm.

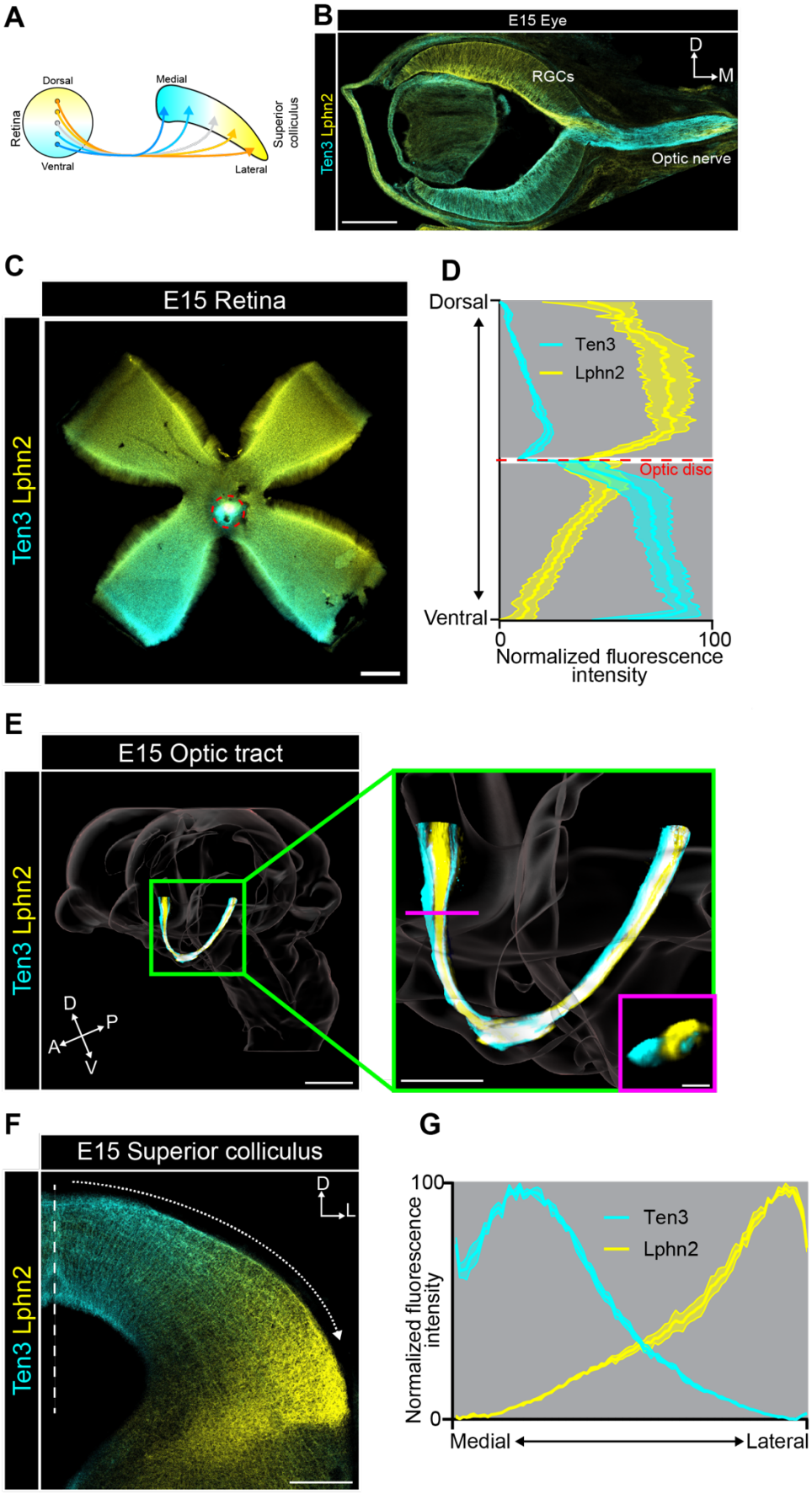

Figure 3. Inverse expression patterns of Ten3 and Lphn2 follow retinotopic connections

(A) Schematic diagram of retinotopic connections from the retina to the superior colliculus along the dorsal–ventral axis of the retina, with Ten3 (cyan) and Lphn2 (yellow) expression from our data superimposed.
(B) Ten3 and Lphn2 protein expression in a single coronal section of the retina. RGCs- Retinal ganglion cells. Scale bar, 200 µm.
(C) Flat whole–mount E15 retina preparation stained for Ten3 and Lphn2 proteins. Red circle indicates optic nerve head, where RGC axons exit the retina. Scale bar, 200 µm.
(D) Quantification of Ten3 and Lphn2 proteins across the dorsal–ventral axis of the retina. See Methods for details on regions analyzed (n = 4 mice; 1 retina/mouse). Mean ± SEM.
(E) 3D reconstruction of E15 optic tract from light sheet microscope images with Ten3 and Lphn2 proteins labeled. Scale bar, 400 µm. Green inset, zoom in of the optic tract. Scale bar 200, µm. Magenta inset, cross section of the optic tract. Scale bar, 50 µm.
(F) Ten3 and Lphn2 protein expression in the superior colliculus in a coronal section of an E15 brain. Dotted lines indicate the axis used for quantification in (G). Vertical dashed line indicates the midline. Dotted arrow indicates the axis used for quantification in (G). Scale bar, 200 µm.
(G) Quantification of Ten3 and Lphn2 protein across the medial–lateral axis of the superior colliculus (n = 3 mice). Mean ± SEM.

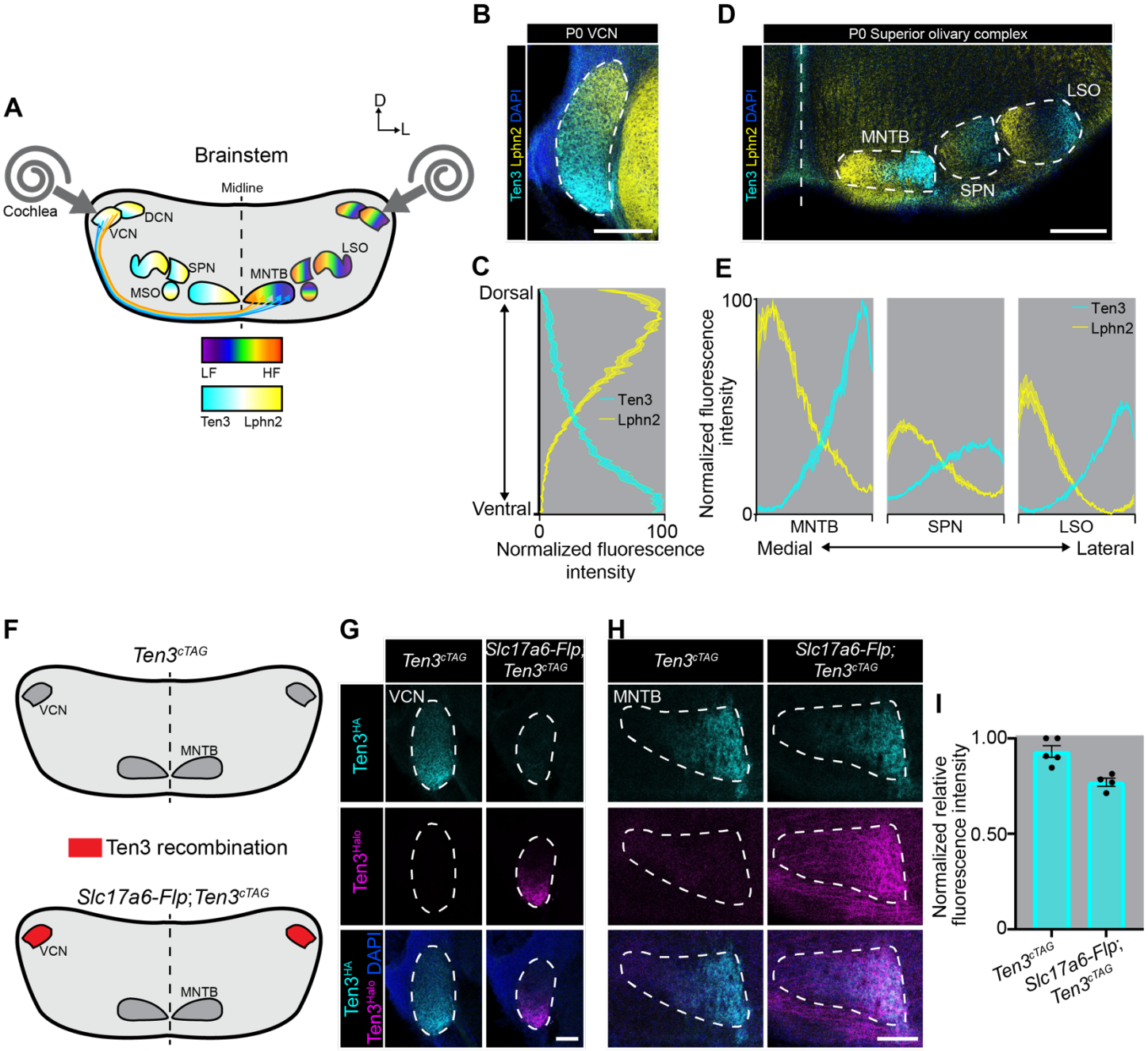

Figure 4. Tonotopic expression of Ten3 and Lphn2 in auditory processing regions of the brainstem.
(A) Schematic diagram of auditory processing nuclei in the brainstem and tonotopic organization represented in a rainbow color spectrum. Cyan and yellow summarize expression patterns of Ten3 and Lphn2 from our data, which align with tonotopic maps across these nuclei. Tonotopic projections from VCN to MNTB are illustrated. DCN, dorsal cochlear nucleus; VCN, ventral cochlear nucleus; MSO, medial superior olive; LSO, lateral superior olive; SPN, superior paraolivary nucleus; MNTB, medial nucleus of the trapezoid body.
(B) Ten3 and Lphn2 protein expression in the VCN of a P0 brain. Scale bar, 200 µm.
(C) Quantification of Ten3 and Lphn2 protein across the dorsal–ventral axis of the VCN (n = 3 mice). Mean ± SEM.
(D) Ten3 and Lphn2 protein expression in the superior olivary complex of a P0 brain. Scale bar, 200 µm.
(E) Quantification of Ten3 and Lphn2 protein across the medial–lateral axis of the superior olivary complex (n = 3 mice). Mean ± SEM.

(F) Schematic diagram depicting spatial patterns of recombination of *Ten3*^{cTAG} allele in the VCN→MNTB projection pathway in the absence (top) and presence (bottom) of *Slc17a6-Flp*.
(G, H) Ten3^{HA} and Ten3^{Halo} protein expression in the VCN (G) and MNTB (H) of *Ten3*$^{cTAG/cTAG}$ and *Slc17a6-Flp;Ten3*$^{cTAG/cTAG}$ P0 mice. Dotted lines denote VCN (G) and MNTB (H). Scale bar, 100 µm.
(I) Quantification of relative HA staining in the MNTB of *Ten3*$^{cTAG/cTAG}$ (n = 5) and *Slc17a6-Flp;Ten3*$^{cTAG/cTAG}$ (n = 4) P0 mice.

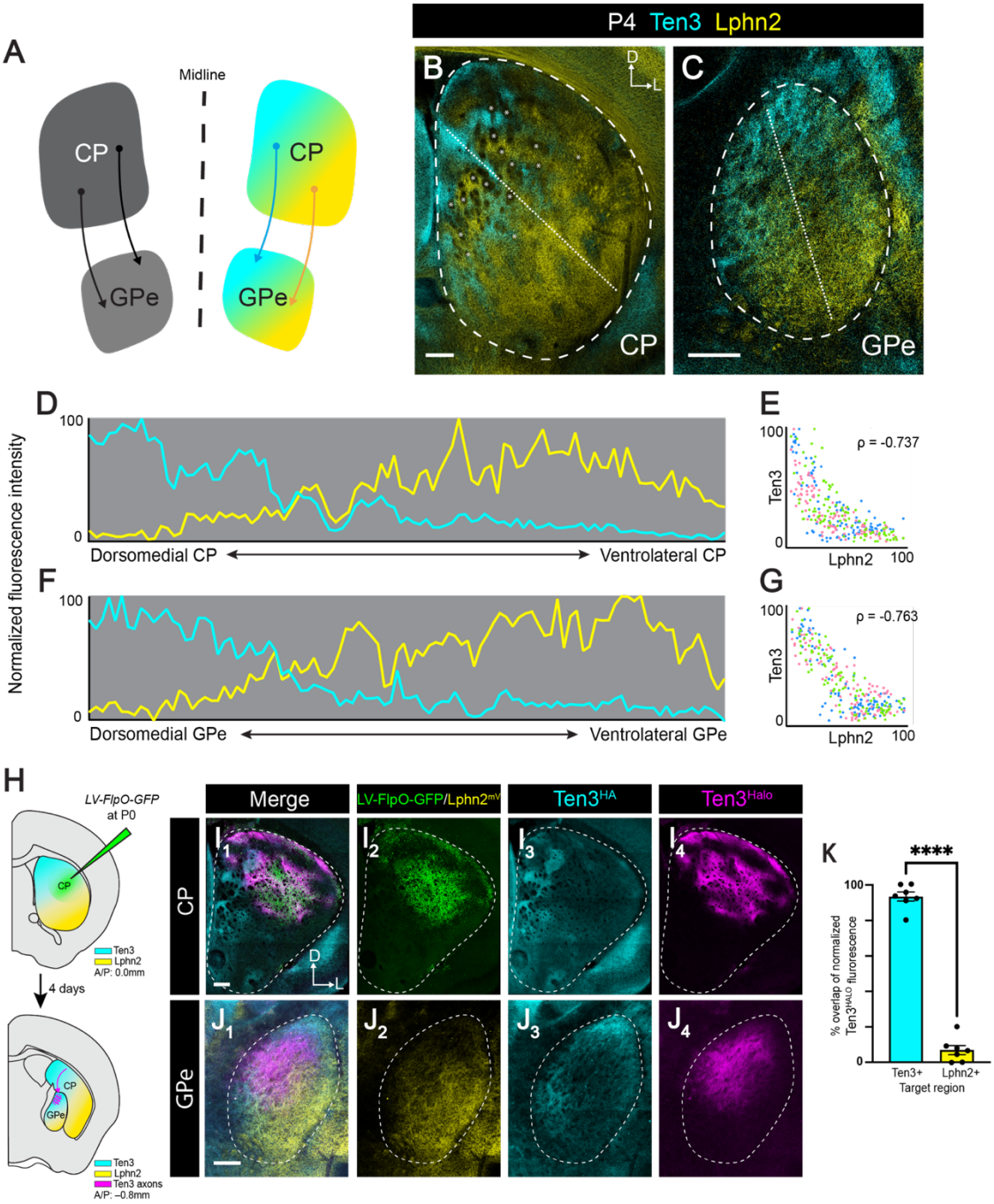

Figure 5. Ten3 and Lphn2 display inverse expression in CP and GPe

(A) Schematic diagram of connections from the caudoputamen (CP) to the globus pallidus external segment (GPe), constituting part of the indirect pathway of the basal ganglia.

(B, C) Ten3 and Lphn2 protein expression in the CP (B) and GPe (C) of a P4 brain, shown in coronal sections. CP and GPe are demarcated by the dashed outlines. Dotted lines indicate the axis used for quantification in (D) and (F). * indicates cortical axon bundles streaming through the CP. Scale bar, 200 µm.

(D) Quantification of Ten3 and Lphn2 protein across the dorsomedial–ventrolateral axis (dotted line in B) of the CP denoted.

(E) Spearman's correlation between Ten3 and Lphn2 expression in the CP (n = 3 mice). Each dot represents the normalized fluorescence intensity of Ten3 and Lphn2 in a single x-y spatial bin (n = 100 bins per brain along the dorsomedial–ventrolateral axis). Individual mice are indicated by color. See STAR Methods for details on analysis.

(F, G) Same as (D, E), except for GPe.

(H) Experimental design and summary of results for tracing CP→GPe connectivity pattern. LV, lentivirus. Recombination of *Ten3*^{cTAG} allele at the injection site causes some Ten3^{HA} CP neurons to express Ten3^{Halo}. Recombined Ten3^{Halo} axons from the CP target GPe regions that express Ten3^{HA}.
(I) Injection site of *LV-FlpO-GFP* in the CP of *Ten3*$^{cTAG/cTAG}$*;Lphn2*$^{mV/mV}$ mice at P4. *LV-FlpO-GFP* injected CP neurons shown in green, Ten3^{HA} in cyan, and Ten3^{Halo} in magenta. Dotted lines outline the CP. Scale bar, 200 µm.
(J) Projection patterns of Ten3^{Halo} CP axons (from injection in penal I) in the GPe. Ten3^{Halo} CP axons target the Ten3^{HA}-high region and avoid Lphn2^{mV}-high region of the GPe. Dotted lines outline the GPe. Scale bar, 200 µm.
(K) Percent overlap of normalized fluorescence of Ten3^{Halo} CP projections to Ten3^{HA} or Lphn2^{mV} GPe target regions in *Ten3*$^{cTAG/cTAG}$*;Lphn2*$^{mV/mV}$ mice at P4 (n = 7). Paired t-test; ****P < 0.0001.

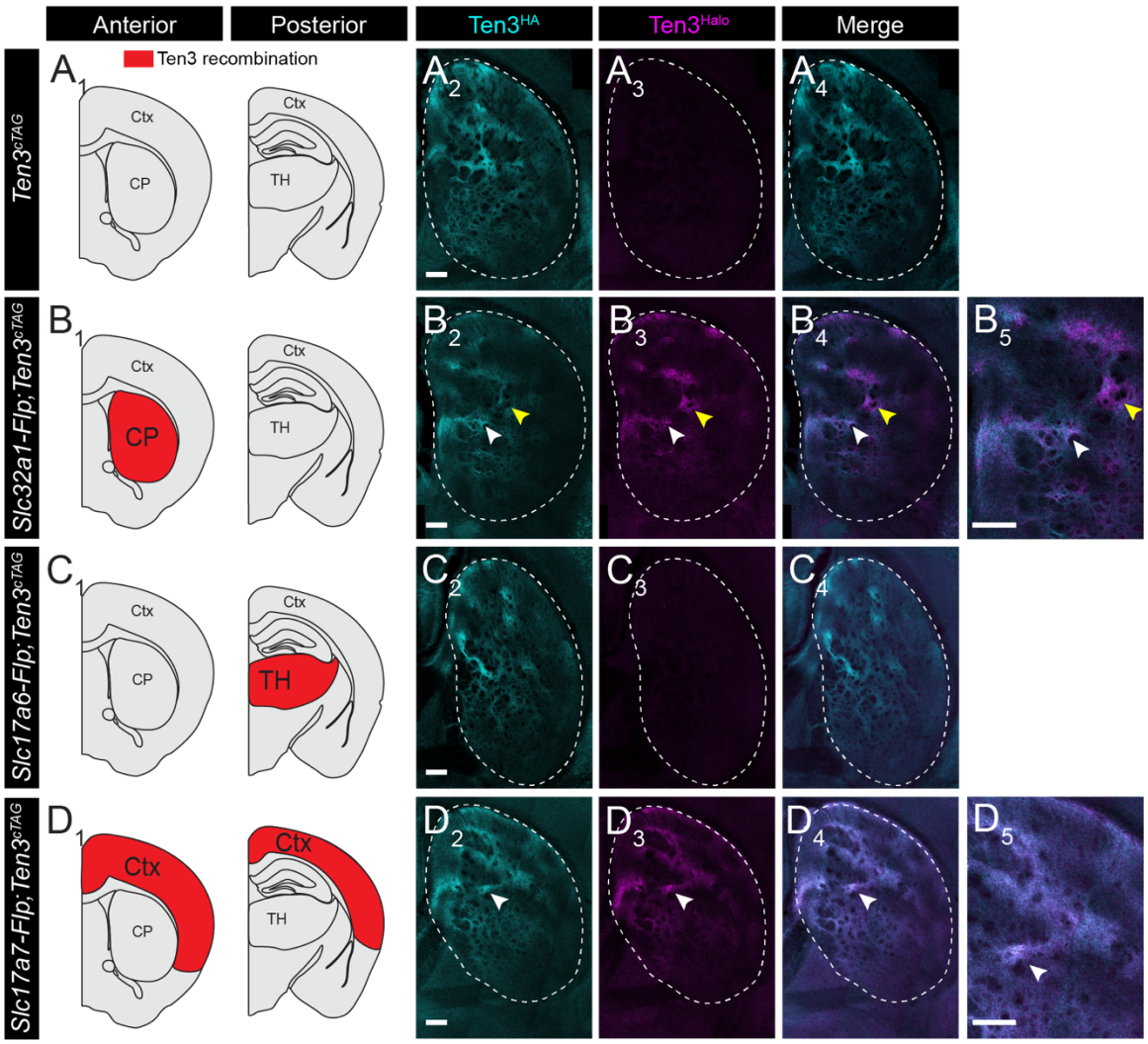

Figure 6. Corticostriatal projections follow the Ten3→Ten3 rule

Left panels are two coronal sections of the mouse brain atlas, with red highlighting regions of recombination due to the expression patterns of the Flp driver. Right panels are experimental data in P4 mice. CP is demarcated by the dashed outlines. Scale bar, 200 µm. Genotypes on the left.

(A) In the absence of Flp driver, Ten3^{HA} but not Ten3^{Halo} protein is expressed in the CP of *Ten3*$^{cTAG/cTAG}$ mice.

(B) In the presence of *Slc32a1-Flp*, which is expressed in all GABAergic neurons, Ten3^{+} CP neurons express Halo. Regions with higher recombination of Ten3^{Halo} indicated by yellow arrows. Persistence of Ten3^{HA} that overlap with Ten3^{Halo} (white arrows) may be from incomplete recombination of GABAergic CP neurons, non-GABAergic Ten3^{+} CP neurons, or input axons from cortex and/or thalamus.

(C) In the presence of *Slc17a6-Flp*, which is expressed in all excitatory neurons in the thalamus, the lack of Halo signal in CP suggests that Ten3^{+} thalamic excitatory neurons do not express Ten3 in their axon terminals at this stage.

(D) In the presence of *Slc17a7-Flp*, which is expressed in all excitatory neurons in the cortex, the overlap between Halo and HA signals in the CP (white arrows) indicates that Ten3^{+} cortical neurons project their axons to Ten3^{+} striatal regions.

Scale bar, 200 µm.

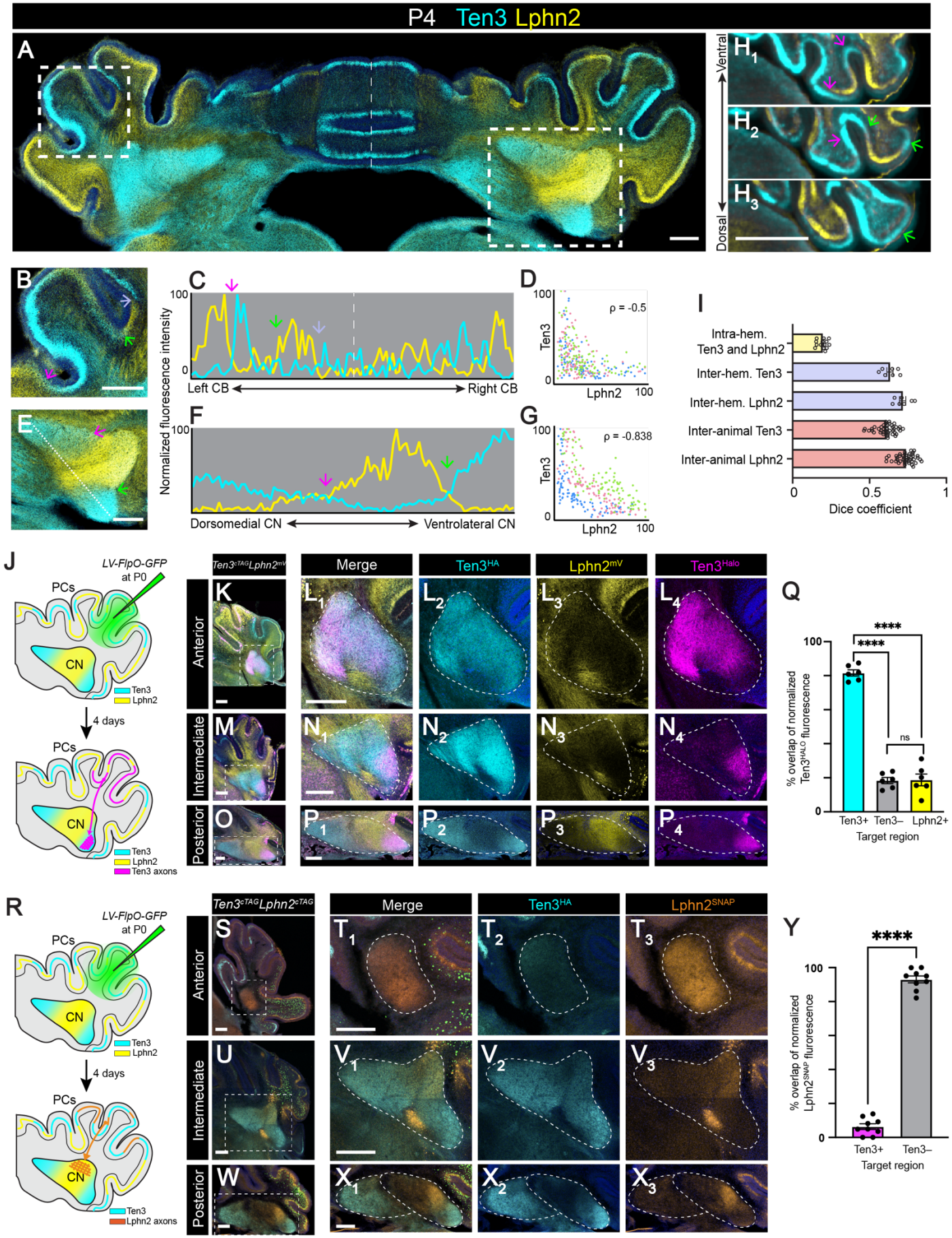

Figure 7. Inverse expression of Ten3 and Lphn2 in both Purkinje cells and cerebellar nuclei

(A) Ten3 and Lphn2 protein expression in the cerebellum of a P4 brain, shown in a coronal section. Scale bar, 500 µm.
(B) Enlarged view of the cerebellar cortical region outlined in (A, left), showing Ten3 and Lphn2 protein expression in the Purkinje cell layer. Different colored arrows denote regions where Ten3 and Lphn2 expression domains shift. Scale bar, 500 µm.
(C) Quantification of normalized Ten3 and Lphn2 protein fluorescence intensity along the PC layer across the left–right axis of the entire cerebellar cortex shown in (A). Different colored arrows indicate the same positions marked by the same colors in (B).
(D) Spearman's correlation between Ten3 and Lphn2 expression in the cerebellar cortex from data in (C); n = 3 mice. Each dot represents the normalized expression level of Ten3 and Lphn2 in a single x-y spatial bin (n = 100 bins per brain along the PC layer). Individual mice are indicated by color (see STAR Methods for detail).
(E–G) Same as (B–D), except for cerebellar nuclei.
(H) Ten3 and Lphn2 protein expression in the cerebellar cortex visualized in serial horizontal sections following iDISCO clearing and whole brain light-sheet imaging. Magenta arrows in H_1 indicate two discrete Ten3-expressing domains that converge in more dorsal plane (H_2). Green arrows in H_2 mark another pair of Ten3 domains that merge further dorsally (H_3). In 3D, both Ten3 and Lphn2 expression form continuous, spatially distinct domains, giving rise to four discrete domains across the cerebellar cortex. Scale bar, 700 µm.
(I) Quantification of spatial stereotypy of Ten3 and Lphn2 expression in the P0 cerebellum using the Dice similarity coefficient. Comparisons include spatial overlap of Ten3 and Lphn2 within the same hemisphere (top), Ten3 or Lphn2 expression across hemispheres of the same brain (2nd and 3rd rows), and inter-animal comparisons of Ten3 and Lphn2 expression patterns (4th and 5th rows). Each dot represents a pairwise comparison; bar represent mean ± SEM.
(J) Experimental design (top) and summary of results (bottom) for tracing $Ten3^{+}$ Purkinje cell (PC)→cerebellar nuclei (CN) connectivity. LV, lentivirus. Recombination of *Ten3*^{cTAG} allele at the injection site causes $Ten3^{+}$ PCs to switch from expressing $Ten3^{HA}$ to $Ten3^{Halo}$. Recombined $Ten3^{Halo}$ axons from the PCs target areas of cerebellar nuclei that express $Ten3^{HA}$. Cerebellar cortex injected at P0.
(K, M, O) Injection sites of *LV-FlpO-GFP* in the cerebellar cortex of *Ten3*$^{cTAG/cTAG}$*;Lphn2*$^{mV/mV}$ mice at P4. Each row indicates an individual mouse. $Ten3^{HA}$ is shown in cyan, *LV-FlpO-GFP* injected CP neurons in green, and $Ten3^{Halo}$ in magenta.
(L, N, P) $Ten3^{HA}$, $Lphn2^{mV}$, and $Ten3^{Halo}$ protein expression in the anterior (L), intermediate (N), and posterior (P) cerebellar nuclei of *Ten3*$^{cTAG/cTAG}$*;Lphn2*$^{mV/mV}$ mice at P4. Panels L_{1-4}, N_{1-4}, and P_{1-4} correspond to dashed box in panels K, M, O, respectively. Dotted lines outline the cerebellar nuclei.
(Q) Percent overlap of normalized fluorescence of $Ten3^{Halo}$ cerebellar cortical projections to $Ten3^{HA}$ positive or negative, or $Lphn2^{mV}$ cerebellar nuclei target areas in *Ten3*$^{cTAG/cTAG}$*;Lphn2*$^{mV/mV}$ mice at P4 (n = 6). Paired t-test; ****P < 0.0001; ns, not significant.
(R) Experimental design (top) and summary of results (bottom) for tracing $Lphn2^{+}$ Purkinje cell→cerebellar nuclei connectivity. LV, lentivirus. Recombination of *Lphn2*^{cTAG} allele at the injection site $Lphn2^{+}$ Purkinje cells switch from expressing $Lphn2^{FLAG}$ to $Lphn2^{SNAP}$. Recombined $Lphn2^{SNAP}$ axons from the cerebellar cortex target $Ten3^{HA}$ negative regions of the cerebellar nuclei. Cerebellar cortex injected at P0.
(S, U, W) Injection sites of *LV-FlpO-GFP* in the cerebellar cortex of *Ten3*$^{cTAG/cTAG}$*;Lphn2*$^{cTAG/cTAG}$ mice at P4. Each row indicates an individual mouse. $Ten3^{HA}$ is shown in cyan, *LV-FlpO-GFP* transduced PCs in green, and $Lphn2^{SNAP}$ in orange.
(T, V, X) $Ten3^{HA}$ and $Lphn2^{SNAP}$ protein expression in the anterior (T), intermediate (V), and posterior (X) cerebellar nuclei of *Ten3*$^{cTAG/cTAG}$*;Lphn2*$^{cTAG/cTAG}$ mice at P4. Panels T_{1-3}, V_{1-3}, and X_{1-3} correspond to dotted box in panels S, U, W, respectively. Dotted lines outline the cerebellar nuclei.
(Y) Percent overlap of normalized fluorescence of $Lphn2^{SNAP}$ cerebellar cortical projections to $Ten3^{HA}$ positive or negative cerebellar nuclei target areas in *Ten3*$^{cTAG/cTAG}$*;Lphn2*$^{cTAG/cTAG}$ mice at P4 (n = 9). Paired t-test; ****P < 0.0001. Scale bar, 200 µm for all panels unless specified.

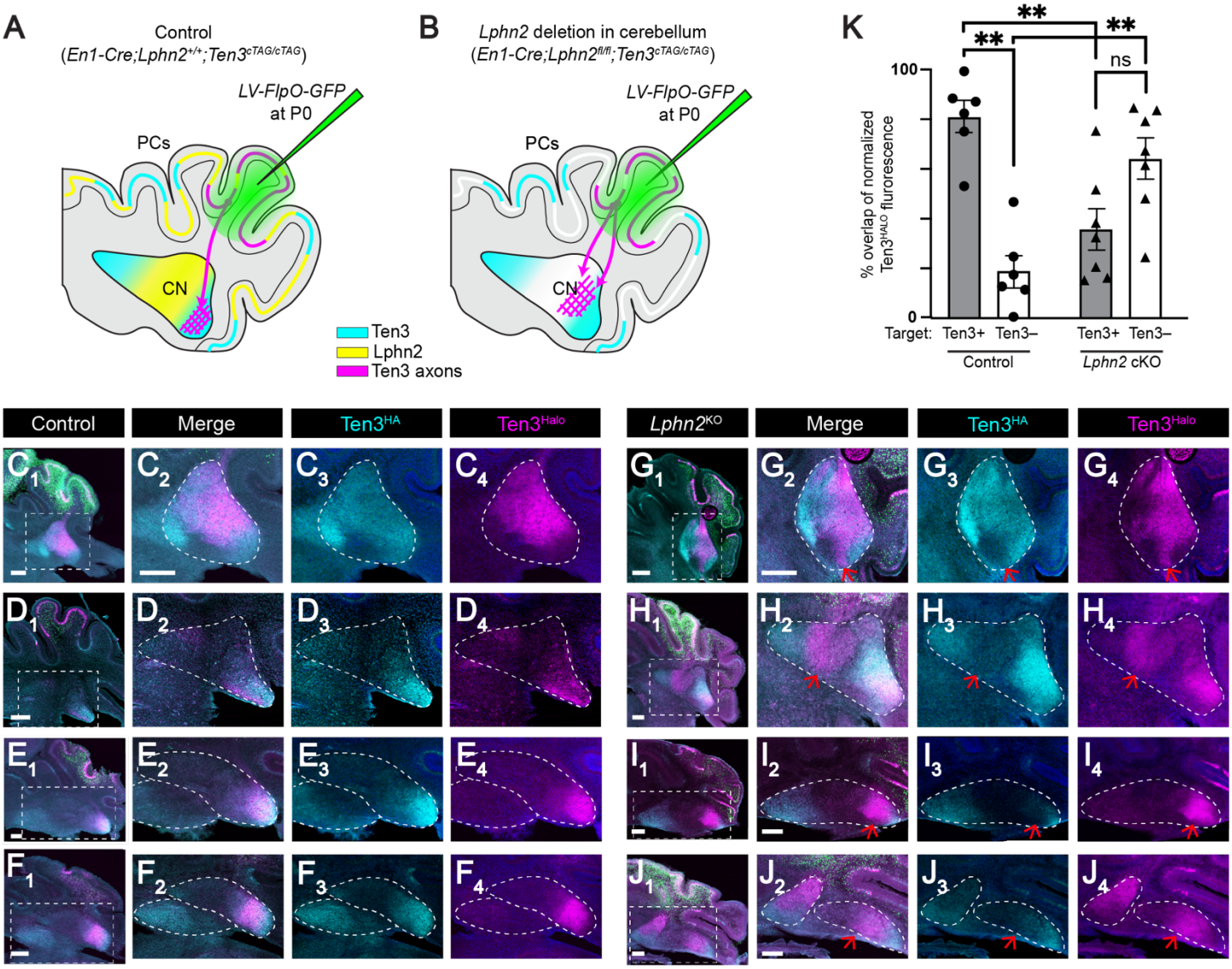

Figure 8. Lphn2 is required for Ten3^{+} Purkinje cell axons to precisely target Ten3^{+} regions of the cerebellar nuclei.

(A, B) Experimental design and summary of results for examining Ten3→Ten3 projection in control (A) and *Lphn2* conditional knockout in the cerebellum (B). LV, lentivirus.

(C–F) Ten3^{HA} and Ten3^{Halo} protein expression in the anterior (C), intermediate (D), and posterior (E & F) cerebellar nuclei of *En1-Cre;Lphn2$^{+/+}$;Ten3$^{cTAG/cTAG}$* mice at P4. Cerebellar cortex of these mice had been injected with *Lenti-FlpO-GFP* (green) at P0.

(G–J) Ten3^{HA} and Ten3^{Halo} protein expression in the anterior (G), intermediate (H), and posterior (I & J) cerebellar nuclei of *En1-Cre;Lphn2$^{fl/fl}$;Ten3$^{cTAG/cTAG}$* mice at P4. Cerebellar cortex of these mice had been injected with *Lenti-FlpO-GFP* (green) at P0. Red arrows indicate mistargeting of Ten3^{Halo} axons in a Ten3^{HA} negative area.

(K) Percent overlap of normalized fluorescence of Ten3^{Halo+} Purkinje cell axonal projections to Ten3^{HA} positive or negative cerebellar nuclei target regions in control (n = 6) and *Lphn2* conditional knockout mice (n = 7) at P4. Paired t-test was performed. **$P < 0.01$. Mean ± SEM.

Scale bar, 200 µm for all panels.

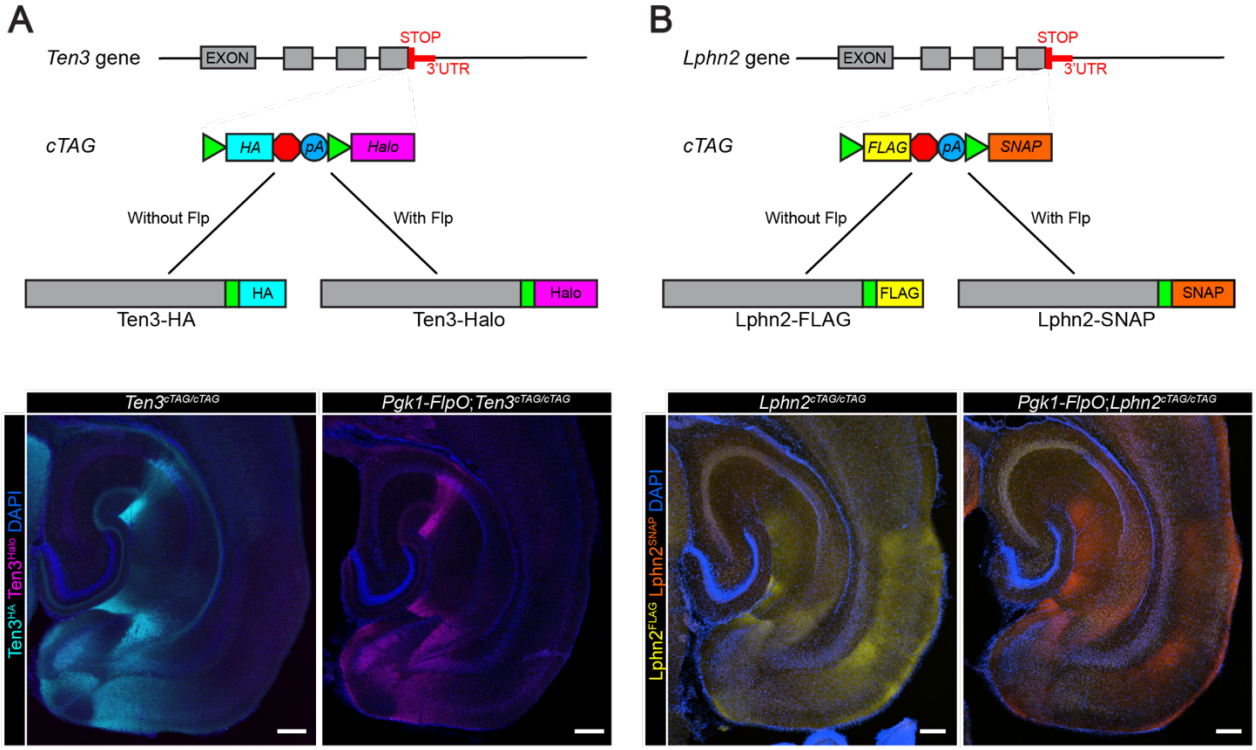

Figure S1. Design of *Ten3*^{cTAG} and *Lphn2*^{cTAG} mice

(A) Schematic of the *Ten3*^{cTAG} mice. To generate the *Ten3* conditional tag mice, an HA epitope tag was added immediately upstream of the STOP codon (red octagon) of the *Ten3* open reading frame, flanked by two *FRT* sites (green triangle), followed by a Halo tag. In the absence of Flp recombinase, Ten3 protein is tagged with HA, and in the presence of Flp recombinase, Ten3 protein is tagged with Halo. Bottom: Ten3 protein expression in a horizontal section across the hippocampal-entorhinal region in a postnatal day 8 (P8) mouse was visualized with anti-HA antibody in the hippocampus of *Ten3*$^{cTAG/cTAG}$ mice (left), and with Halo tag ligand in the same area in *Pgk1-FlpO;Ten3*$^{cTAG/cTAG}$ mice. Both samples are double stained with HA and Halo tag ligand, demonstrating lack of Halo signal in the absence of Flp and complete conversion of HA into Halo in the presence of Flp.

(B) Same as (A) except for the *Lphn2*^{cTAG} mice. In the absence of Flp recombinase, Lphn2 is tagged with a FLAG tag; in the presence of Flp recombinase, Lphn2 is tagged with a SNAP tag.

Scale bar, 200 µm.

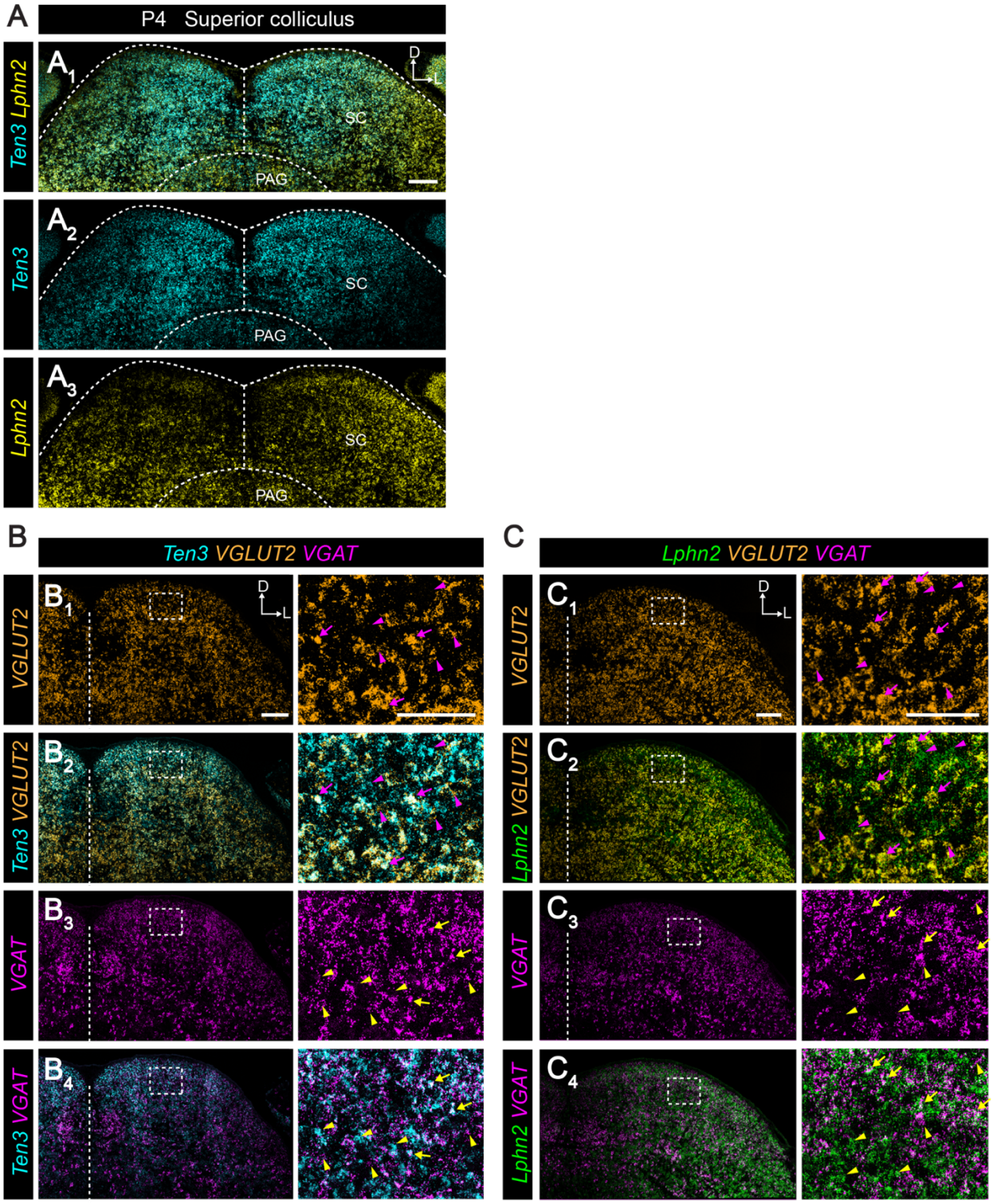

Figure S2. *Ten3* and *Lphn2* mRNA display inverse expression in the superior colliculus

(A) *Ten3* and *Lphn2* mRNA expression in a single coronal section of the superior colliculus at postnatal day 4 (P4).

(B, C) Co-expression analysis of *Ten3* mRNA (B) and *Lphn2* mRNA (C) with *VGLUT2* and *VGAT* mRNA, markers for excitatory and inhibitory neurons, respectively. In the high-magnification insets (correspond to the dashed rectangles to the left), arrows point to cells co-expressing *Ten3* or *Lphn2* and *VGLUT2* or *VGAT*. Side arrowheads point to cells only expressing either *Ten3* mRNA (B) or *Lphn2* mRNA (C). Upward arrowheads point to cells only expressing either *VGLUT2* mRNA (top two panels) or *VGAT* mRNA (bottom two panels). Thus, both *Ten3* and *Lphn2* are expressed in both excitatory and inhibitory neurons.

Vertical dashed line indicates the midline. Scale bar, 200 µm (Inset 100 µm) unless specified.

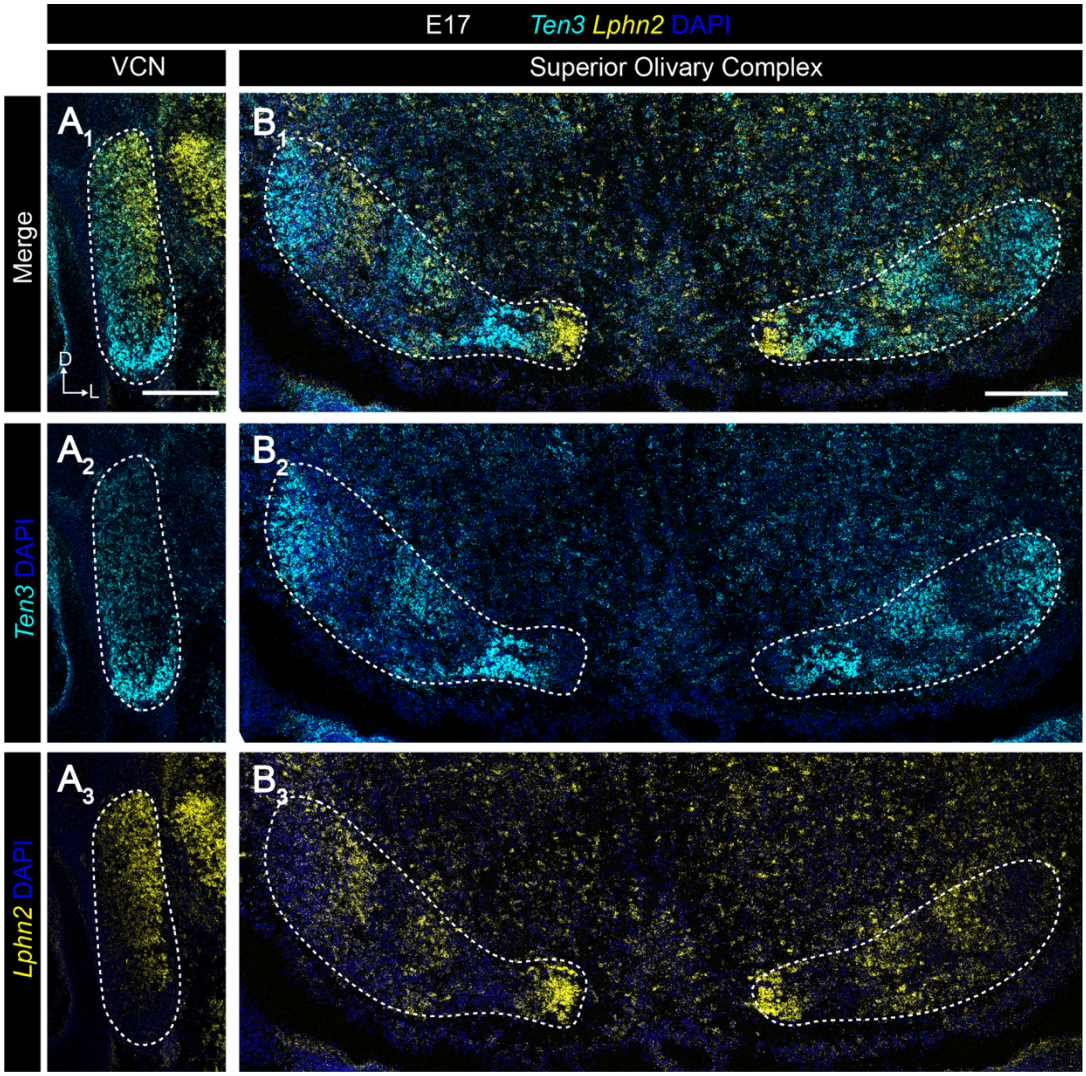

Figure S3. *Ten3* and *Lphn2* mRNA display inverse expression in the auditory brainstem nuclei
Ten3 and *Lphn2* mRNA expression in a single coronal section of the ventral cochlear nucleus (VCN; A) and the nuclei of the superior olivary complex (B) at E17. VCN and superior olivary complex are demarcated by the dashed outlines. Scale bar, 200 µm.

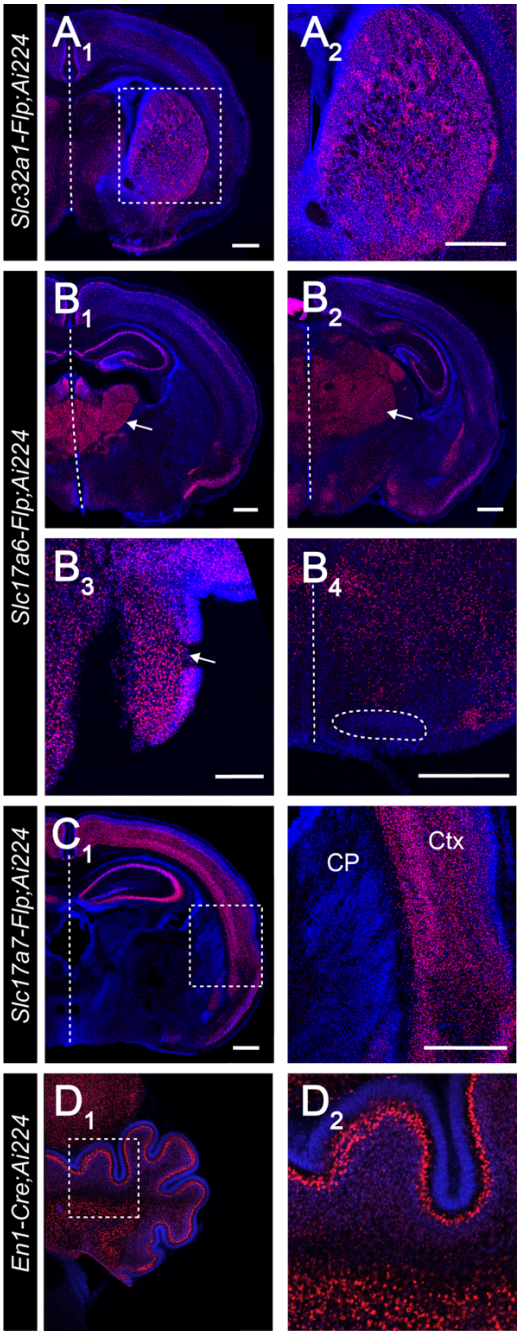

Figure S4. Validation of Flp and Cre driver lines

(A) Coronal section of *Slc32a1-Flp;Ai224* at P4 showing labeled GABAergic neurons in the CP. *Ai224* is a Flp-dependent nuclear tdTomato reporter line. A_2 is a higher-magnified view of the white dashed box in A_1, highlighting labeled GABAergic neurons within CP.

(B) Coronal sections of *Slc17a6-Flp;Ai224* at P4 showing labeled excitatory neurons in the anterior (B_1, arrow) and posterior thalamus (B_2, arrow). Cells in the ventral cochlear nucleus (arrow) are also labeled (B_3) but cells in the medial nucleus of the trapezoid body of the superior olivary complex demarcated by the dashed outlines are not labeled (B_4).

(C) Coronal section of *Slc17a7-Flp;Ai224* at P4 showing labeled excitatory neurons in the cortex. C_2 is a higher-magnified view of the white dashed box in C_1, highlighting labeled excitatory neurons within the hippocampus (arrowhead) and the cortex (arrow).

(D) Coronal section of *En1-Cre;Ai224* at P4 showing labeled Purkinje cells and the neurons in the cerebellar nuclei. D_2 is a higher-magnified view of the white dashed box in D_1, highlighting labeled neurons within the cerebellar nuclei (arrow) and the Purkinje cell layer (arrowhead).

CP– Caudate putamen; Ctx– Cortex. Scale bar, 500 µm (100 µm for B_3).

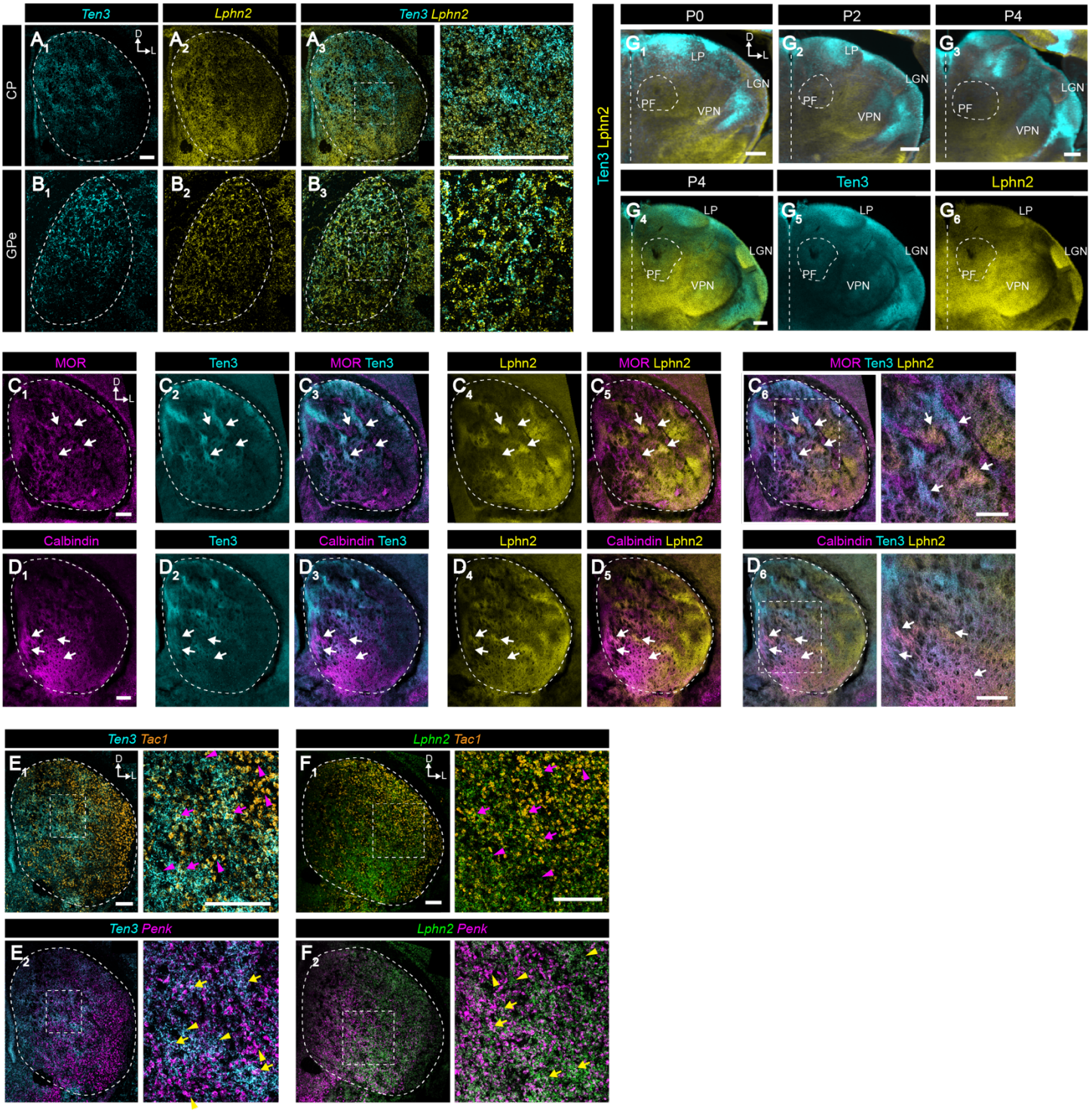

Figure S5. *Ten3* and *Lphn2* mRNA display inverse expression in CP and GPe

(A, B) *Ten3* and *Lphn2* mRNA expression in the CP (A) and GPe (B) of a P4 brain, shown in coronal sections. CP and GPe are demarcated by the dashed outlines based on DAPI co-staining (not shown). High-magnification insets correspond to the dashed rectangles in the left panel.

(C, D) Co-expression analysis of Ten3 and Lphn2 with μ-opioid receptor (MOR, C) or calbindin (D), markers of striosomes and extrastriosomal matrix, respectively. High-magnification insets correspond to the dashed rectangles in the left panel (C_4). Arrows point to cells co-expressing *Ten3* or *Lphn2* and MOR^+ (C) or $Calbindin^+$ (D) CP regions. A subset of MOR^+ regions overlapped with either $Ten3^+$ and $Lphn2^+$ domains, and similarly, some $Calbindin^+$ regions comprised regions overlapping with either Ten3 or Lphn2 expression. Thus, *Ten3* and *Lphn2* are expressed in both striosome and matrix regions of the CP.

(E, F) *Ten3* and *Lphn2* mRNA expression in the CP does not align with *Tac1* or *Penk* mRNA expression. Arrows point to overlapping regions. Side arrowheads point to cells exclusively expressing either *Ten3* mRNA (E) or *Lphn2* mRNA (F). Upward arrowheads point to cells exclusively expressing either *Tac1* mRNA (top panels) or *Penk* mRNA (bottom panels).
(G) Ten3 and Lphn2 protein expression in the thalamus at P0, 2 and 4. Note that parafascicular nucleus, a nucleus that is known to project axons to the CP, does not express high levels of Ten3 protein during development.
Scale bar, 200 μm.

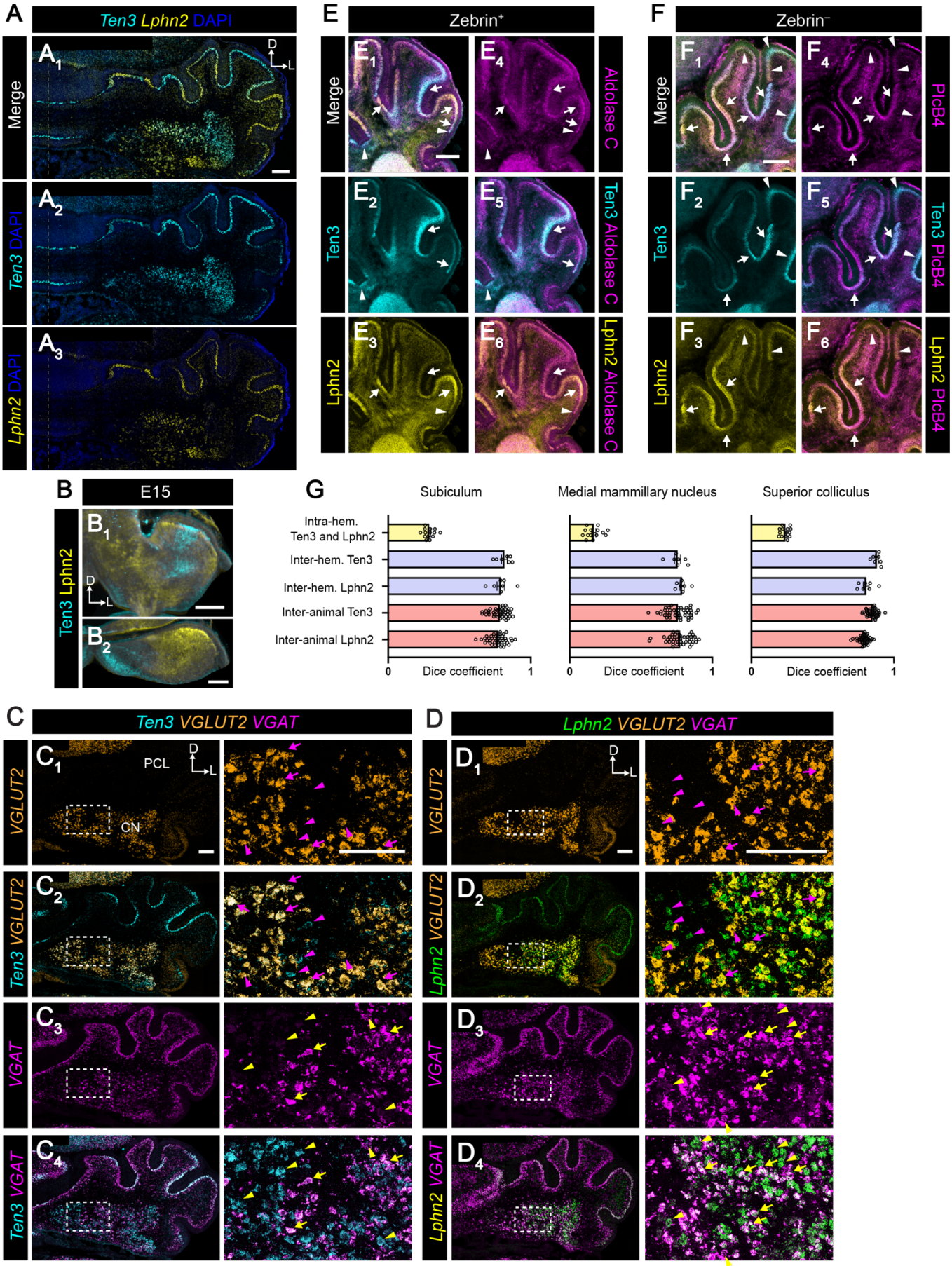

Figure S6. ***Ten3*** **and** ***Lphn2*** **mRNA and proteins co-expression analysis**

(A) *Ten3* and *Lphn2* mRNA expression in the cerebellum of a P4 brain, shown in a coronal section, showing their inverse expression along the medial–lateral axis.
(B) Ten3 and Lphn2 protein expression in the cerebellum of a E15 brain, visualized by whole brain immunostaining and light-sheet microscopy (B_1- anterior section) and immunohistochemistry followed by confocal microscopy (B_2- posterior section). Even at this early stage, Ten3 and Lphn2 exhibit continuous 3D expression pattern that can be segmented into four discrete domains per hemisphere, indicating early establishment of spatial organization. This organization is observed in the anterior cerebellar cortex (B_1), whereas in the posterior cerebellar cortex, the expression is segregated into two broad domains with medial expression of Ten3 and lateral expression of Lphn2 (B_2).
(C, D) Co-expression of *Ten3* mRNA (C) or *Lphn2* mRNA (D) with both *VGLUT2* or *VGAT* mRNA, markers for excitatory or inhibitory neurons, respectively, in the cerebellar nuclei. In high-magnification insets, arrows point to cells that co-express *Ten3* or *Lphn2* with either *VGLUT2* or *VGAT*. Side arrowheads point to cells only expressing either *Ten3* mRNA (C) or *Lphn2* mRNA (D). Upward arrowheads point to cells only expressing either *VGLUT2* mRNA (top two panels) or *VGAT* mRNA (bottom two panels). A subset of *VGLUT2*$^+$ regions overlapped with either *Ten3*$^+$ and *Lphn2*$^+$ domains, and similarly, a subset of *VGAT*$^+$ regions comprised regions overlapping with either *Ten3* or *Lphn2* expression. These data indicate that both *Ten3* and *Lphn2* are expressed in both glutamatergic and GABAergic neurons.
(E, F) Ten3 and Lphn2 protein expression in the cerebellum of a P4 brain partially overlap with both aldolase C (E) and PlcB4 (F), zebrin-positive and negative markers, respectively. Arrows indicate regions where either Ten3 or Lphn2 expression overlaps with zebrin$^+$ (E) or zebrin$^-$ (F) markers, and arrowheads indicate where either Ten3 or Lphn2 expression does not overlap with zebrin$^+$ (E) or zebrin$^-$ (F) markers. A subset of Aldolase C$^+$ regions overlapped with either Ten3$^+$ and Lphn2$^+$ domains, and similarly, a subset of Plcb4$^+$ regions comprised regions overlapping with either Ten3 or Lphn2 expression. These data indicate that both Ten3 and Lphn2 are expressed in both zebrin$^+$ and zebrin$^-$ neurons.
(G) Quantification of spatial stereotypy of Ten3 and Lphn2 expression in the P0 subiculum, medial mammillary nucleus, and the superior colliculus using the Dice similarity coefficient. Comparisons include spatial overlap of Ten3 and Lphn2 within the same hemisphere (top), Ten3 or Lphn2 expression across hemispheres of the same brain (2nd and 3rd rows), and inter-animal comparisons of Ten3 and Lphn2 expression patterns (4th and 5th rows). Each dot represents a pairwise comparison; bar represent mean ± SEM.
PCL- Purkinje cell layer; CN- cerebellar nuclei. Scale bar, 200 µm.

METHODS

Animals

All animal procedures followed animal care guidelines approved by Stanford University's Administrative Panel on Laboratory Animal Care and Administrative Panel on Biosafety in accordance with NIH guidelines. Both male and female animals were used, where they were group housed with access to food and water *ad libitum*.

Slc32a1-Flp (Jackson Laboratory, Stock 029591), *Slc17a6-Flp* (Jackson Laboratory, Stock 030212), and *Slc17a7-Flp* (Jackson Laboratory, Stock 034422) were bred to used Ten3^{cTAG} to recombine *Ten3* allele. *En1-Cre* (Jackson Laboratory, Stock 007916) mice[116], and Lphn2^{mVenus} and Lphn2$^{fl/fl}$ mice[28] were on a C57BL/6 and 129 mixed background and were backcrossed to wild-type CD1 mice to improve pup survival rate. All genotyping was performed as previously described[23,24,28,116].

Generation of conditional tagged mice

Ten3 and Lphn2 conditional tag (cTAG) mice were generated by the Gene Targeting and Transgenics core at Janelia Research Campus. Both mouse lines were generated by homologous recombination in ES cells using standard procedures. For Ten3 conditional tag mice, an HA tag was added immediately upstream of the STOP codon flanked by two FRT sites, followed by a HALO tag. For Lphn2 conditional tag mice, a FLAG tag was added immediately upstream of the STOP codon flanked by two FRT sites, followed by a SNAP tag. Targeting was verified in ES cells by long-arm PCR. After microinjection, chimeras were bred to CD1 females and F1 offspring were screened by long-arm PCR and Southern blot to identify animals with germline transmission of the correctly targeted construct.

Genotyping

Primers used for genotyping Ten3^{HA} and Ten3^{Halo} alleles include Ten3-HA-F (CTACGATGGGTACTACGTAC), Ten3-HA-R (GTGGTTTGTCCAAACTCATCA), Ten3-Halo-F (GGTCTGAATCTGCTGCAAGA), and Ten3-R (TCCAGTCCAATTGAGTGCAG). The following oligonucleotide combinations were used to detect the presence of different alleles: Ten3-HA-F/Ten3-HA-R/Ten3-R (WT: 329bp; Ten3^{HA}: 218bp), and Ten3-Halo-F/Ten3-R (Ten3^{Halo}: 361bp). Primers used for genotyping Lphn2^{FLAG} and Lphn2^{SNAP} alleles include Lphn2-FLAG-F (AAGTATGCCCAACCTTGGAG), Lphn2-FLAG-R (CGTCGTCATCCTTGTAATCG), Lphn2-SNAP-F (GGCTGGGTTAATGTCGACAT), and Lphn2-R (TCACAGGACTGTGAGGTTCA). The following oligonucleotide combinations were used to detect the presence of different alleles: Lphn2-FLAG-F/Lphn2-FLAG-R/Lphn2-R (WT: 324bp; Lphn2^{FLAG}: 221bp), and Lphn2-SNAP-F/Lphn2-R (Lphn2^{SNAP}: 223bp).

Whole brain immunolabeling and clearing

Mice were injected with 2.5% avertin and were transcardially perfused with cold phosphate buffered saline (PBS) and 4% paraformaldehyde (PFA). Dissected brains were post-fixed with 4% PFA for at room temperature for 1 hour. Whole brain immunolabeling and clearing was performed using a modified iDISCO protocol.[29,30] Brains were dehydrated through a graded methanol (MeOH) series in B1N buffer, at 20%, 40%, 60%, and 80% MeOH, followed by three washes in 100% MeOH. The incubation time for the dehydration steps were 45 minutes for embryonic brains and 1 hour for postnatal brains. Brains were then incubated overnight in a 2:1 dichloromethane (DCM):MeOH mixture at room temperature. On the next day, they were washed in 100% DCM and 100% MeOH (three times), before incubation in 1:5 H_2O_2/MeOH mixture at room temperature. The brains then went through rehydration in the reverse MeOH gradient in B1N buffer. The brains were then incubated in 5% DMSO/0.3M Glycine/PTxwH (10% Triton X–100, Tween-20, heparin, 5% NaN_3 in PBS) twice for efficient penetration of primary antibodies.

For immunostaining, brains were incubated with primary antibodies– rabbit anti-HA (1:300, Cell Signaling Technology, 3724S) and chicken anti-GFP (1:1000, Aves Labs, GFP-1020) in PTxwH for 5 days (embryonic brains, E15 and E17), 8 days (early postnatal brains, P0–P4), or 11 days (late postnatal and adult brains, P8–P42) brains, at 37°C. After three days of washing in PTxwH, the brains were then transferred into secondary antibodies– donkey anti-rabbit Alexa Fluor 555 (ThermoFisher, A32794) and donkey anti-chicken Alexa Fluor 647 (ThermoFisher, A78952) at 37°C for 4, 6, or 8 days for embryonic, early postnatal, or late

postnatal/adult brains, respectively. Following secondary antibody incubation, the brains were washed in PTxwH for 3 days and PBS for 1 day.

For tissue clearing, brains were dehydrated through a graded MeOH series in water, washed three times in 100% MeOH, and incubated overnight in 2:1 DCM:MeOH mixture. Samples were then washed three times in 100% DCM before being cleared in dibenzyl ether (DBE). The cleared brains were subsequently washed daily in ethyl cinnamate for a minimum of three days prior to imaging.

Light–sheet imaging, registration and dice coefficient analysis

Cleared whole brains were imaged using UltraMicroscope Blaze light–sheet microscope (Miltenyi Biotec) at 1x magnification. We acquired a series of images using three channels (488 nm for autofluorescence, 560 nm for Ten3, and 640 nm for Lphn2) with dynamic focusing for Ten3 and Lphn2 channels at a z-step size of 3 µm. Autofluorescence channel was imaged without dynamic focusing. Voxel sizes were 3.55 µm x 3.55 µm for E15 brains, and 5.91 µm x 5.91 µm for E17 and postnatal brains. Raw image stacks were first downsampled four times, resulting in a voxel size of 23.64 µm x 23.64 µm x 12 µm. Local Ten3- and Lphn2-positive voxels were binarized using Ilastik.[117] We note that the segmentation models were optimized for each region of interest (ROI) by training them with local signal information.

For registration, we first chose one brain from the seven imaged brains as our reference brain. This brain had the qualitatively cleanest signals (e.g., least artifacts and deformation). On the right hemisphere of the reference brain, 3-dimensional ROI masks were prepared using a transformer-based segmentation tool[118] with a combination of the three imaging channels. The other six brains were then registered to this reference brain via non-linear transformation.[119] For inter-hemisphere analysis within the same brains, we reflected the brain with respect to its anterior-posterior axis and performed registration against the non-reflected brain to minimize variations in region boundaries. Finally, signal overlaps were quantified using Dice coefficients (MATLAB).

Immunohistochemistry

Mice were injected with 2.5% Avertin and were trascardially perfused with PBS followed by 4% PFA. Dissected brains were post-fixed with 4% PFA at room temperature for 1 hour, and then cryoprotected in 30% sucrose for 2-3 days. Brains were then embedded in OCT (Tissue-Tek), frozen in isopentane bath that was cooled on dry ice and stored at –20°C until sectioning. Using a cryostat, the frozen brains were sectioned at 60 µm thickness into PBS and stored at 4°C. Immunohistochemistry were performed as previously described.[24] Briefly, the sections were incubated in 10% NDST (0.3% Triton X–100 in PBS and 10% normal donkey serum) for two hours at room temperature, followed by incubation with primary antibodies in 5% NDST (0.3% Triton X–100 in PBS and 5% normal donkey serum) for two nights at 4°C. After multiple washes in PBST (0.3% Triton X–100 in PBS), the sections were incubated with secondary antibodies (1:500) in 5% NDST and DAPI. Sections were mounted with Fluoromount-G (SouthernBiotech, 0100-01) after multiple washes in PBST and PBS. Primary antibodies used were rabbit anti-HA (1:300, Cell Signaling Technology, 3724S), chicken anti-GFP (1:1000, Aves Labs, GFP-1020), rabbit anti-HaloTag (1:500, Promega, G9281), rabbit anti-FLAG-tag (1:1000, Abcam, ab1162), guinea pig anti-Calbindin (1:500, Synaptic Systems, 214004), rabbit anti-MOR (1:500, ImmunoStar, 24216), rabbit anti-Aldolase C (1:300, Abcam, ab115212), and mouse anti-PlcB4 (1:500, Santa Cruz Biotechnology, sc166131). Monoclonal antibody HA-tag–AF-555 (1:300, ThermoFisher, 26183-A555) and SNAP–Surface-549 (1:300, NEB, S9112S) were used. For rabbit anti-FLAG-tag, the antibody was pre–adsorbed on wild–type tissue prior to performing standard immunohistochemistry. Pre-adsorption followed the same immunohistochemistry procedure as stated above. Secondary antibodies conjugated to Alexa 488, 567, Cy3, or 647 (Jackson ImmunoResearch) were used at 1:500 from 50% glycerol stocks. Sections were imaged using the tile scan function on Zeiss LSM 900 confocal microscope with 10x magnification.

Double *in situ* hybridization

Pups of postnatal day 4 (P4) or younger were anesthetized on ice for 1-2 minutes, whereas older mice were injected with 2.5% Avertin. Mice were euthanized by decapitation and were rapidly dissected into cold PBS. The brains were then embedded into Optimum Cutting Temperature (OCT, Tissue–Tek), snap frozen in dry ice–cooled isopentane and stored in –20°C until sectioning. All samples were processed within 1 minute of dissection to

preserve RNA integrity. The fresh–frozen brains were sectioned at 10 µm thickness using a cryostat and mounted onto Superfrost Plus slides (VWR). In situ hybridization was performed using the RNAscope® Multiplex Fluorescent Reagent Kit v2 (ACD Bio) following the manufacturer's protocol.[120] Briefly, sections were fixed in 4% PFA for 2 hours at RT, dehydrated in graded ethanol, and treated with Protease IV. Following target-specific probes from ACD Bio were used: *Ten3* (411951), *Lphn2*-C1 (319341), *Lphn2*-C2 (319341-C2), *Tac1* (410351-C2), *Penk* (318761-C3), *Slc17a6* (319171-C2), and *Slc32a1*(319191-C3). The sections were hybridized with these probes for 2 h at 40°C, followed by signal amplification and detection using Opal fluorophores (Akoya Biosciences; Opal 520, 570, and 650; 1:1500 dilution). Sections were counterstained with DAPI, washed, and mounted in ProLong Gold Antifade Mountant (ThermoFisher, P36930). Sections were imaged using the tile scan function on Zeiss LSM 900 confocal microscope (10x magnification) with identical acquisition settings across samples in the same batch of experiments.

Image Analysis

Fluorescence intensity profiles for Ten3 and Lphn2 were obtained from coronal sections of P4 brains in the CP and GPe (Figures 5B and C), as well as the Purkinje cell layer and the cerebellar nuclei (Figure 7B and E). For each image, ROIs were manually delineated based on anatomical boundaries visible in the DAPI channel. Axes used for quantification were indicated using the dotted lines in Figures 5B, 5C, and 7E. The Purkinje cell layer across the left–right axis of the entire cerebellar cortex was quantified. Mean fluorescence intensity values were extracted along these axes for both Ten3 and Lphn2 channels. To enable direct quantitative comparison across animals, intensity profiles were resampled into 100 equally spaced bins along the axis using a custom MATLAB code previously reported (MathWorks)[24]. Each bin represented the normalized mean fluorescence intensity within its corresponding spatial segment. These binned intensity values were then used for correlation analysis. Spearman's correlation coefficients were computed in R, with each brain region analyzed independently (n = 3 mice each). Data points in the scatterplots correspond to a single x–y bin, and individual mice are indicated by distinct colors.

For spatial quantification of Ten3 and Lphn2 in Figure 3G, 4C and 4E a 200-pixel-wide segmented line was drawn through the cell body layer from each end of the region of interest. These areas were defined by anatomical features or DAPI staining. Segmented lines were drawn, straightened using the Straighten function, background subtraction was performed using the Subtract function and intensity values were measured using the Plot Profile command (performed in FIJI). The intensity plots were resampled into 100 equal bins (MATLAB) and each individual trace was normalized to a maximum of 100. Traces from each mouse were averaged, normalized to a maximum of 100 again and then the normalized average trace from each mouse was combined to give the final distribution.

For relative expression analysis in Figure 2 the following method was used. Sections were stained in three batches, with each batch containing one animal of each age. All images from a region of interest in a batch were imaged using a Zeiss LSM 900 confocal microscope on the same day using the same settings. To quantify relative expression levels regions of interest were drawn using anatomical features, and fluorescent intensity values were obtained using the Histogram tool (performed in FIJI). The mean expression level was calculated for the top 10% of pixels in each image and averaged with all other values from the same region of that animal. Averages were then normalized to the age with the highest expression value. Normalized values were grouped by age and region and plotted in Prism 10 (GraphPad).

Lentivirus production

Lentivirus UBC Cre-GFP was modified such that Cre-GFP was removed and FlpO-Green Lantern was inserted immediately downstream of the UBC promoter using Gibson assembly. Correct insertion of plasmid was verified by whole plasmid sequencing (Plasmidsaurus). Recombinant vectors were generated by transient transfection of 293T cells. The supernatant was harvested 72 hours post-transfection, filtered through a 0.45 µm membrane, and concentrated via ultracentrifugation (18,000 rpm, 2 h, 4°C; SW 32 Ti rotor). Pellets were pooled, resuspended in 3.5 mL DPBS, and further purified by sucrose cushion ultracentrifugation (20% sucrose

cushion, 18,000 rpm, 2 h, 4°C; SW 55 Ti rotor). Final pellets were resuspended in DPBS containing 0.001% pluronic F-68, aliquoted (10 µL), and stored at −80°C.

Stereotactic injections in neonatal mice

All stereotactic injections were performed on P0 mice. Pups were anesthetized by hypothermia on ice for 2-3 minutes, placed in the stereotaxic frame (Stoelting), and injected with 500nL (striatum) or 300uL (cerebellum) of virus per site at 100nL/min using a pulled glass micropipette (Drummond). *LV-FlpO-GFP* was diluted 1:10 from the original viral stock (1.01×10^{13} copies per mL, Boston Children's Hospital Vector Core). Injection coordinates were determined relative to lambda. Striatum injections were 2.0 mm anterior, 1.3 mm lateral, and 1mm ventral from lambda. Cerebellum injections were 3 mm and 2.8 mm anterior (2 injections), 1.8 lateral, and 0.5mm ventral from lambda. After injection, pups were placed on a warm heating pad for recovery before being returned to their home cage. All injections were verified by post hoc analysis.

Ten3→Ten3, Lphn2→Lphn2 projection mapping analysis

Mice were only included if they met the following criteria: 1) lentivirus injections must be specifically in the striatum for experiments described in Figure 5, or the cerebellar nuclei for experiments described in Figure 7; 2) axons projecting to the target region must be at the border of target Ten3–Lphn2 expression; 3) more than three sections per animal needs to have sufficient expression of $Ten3^{Halo}$ or $Lphn2^{SNAP}$ axons at the target region for quantification. Mice that fulfilled these criteria are reported in Figures 5 and 7 and were included in quantifications. Confocal images of sections were acquired using tile function on the Zeiss LSM 900 confocal microscope with identical acquisition settings for all samples within an animal. To account for variability of injection sites between mice, exposure settings were adjusted individually to prevent signal saturation. Projection patterns were quantified using ImageJ/Fiji.

To quantify the overlap of $Ten3^{Halo+}$ or $Lphn2^{SNAP+}$ axons at $Ten3^{HA+}$ target region, ROIs were manually delineated on the DAPI channel using anatomical landmarks. These ROIs were extracted using the clear outside function in ImageJ/Fiji. For each channel, false–positive values were subtracted, and signal thresholds were individually adjusted. A Gaussian blur (radius = 10) was applied, after which ROIs were converted to masks. Image calculator was then used to compute the number of overlapping pixels across all signal channels. Statistical analyses were performed using paired t-tests using Prism 10 (GraphPad).

Lphn2-mediated PC→CN wiring analysis

Overlap of $Ten3^{Halo+}$ axons and $Ten3^{HA+}$ target region in En1-Cre;$Lphn2^{+/+}$;$Ten3^{cTAG/cTAG}$ and En1-Cre;$Lphn2^{fl/fl}$;$Ten3^{cTAG/cTAG}$ mice were quantified using the same inclusion criteria, imaging procedures, and imaging processing methods described above. Following mask conversion, the Halo channel region was scaled down by 75% of its original size and shape from the center, and the outer 25% area along the Ten3–Lphn2 border was isolated and extracted using the clear function. Corresponding regions in other channels were extracted, and Image Calculator was used to determine the number of overlapping pixels across all signal channels. Statistical analyses were performed as previously described, and all quantification was performed by an experimenter blinded to genotype.

ADDITIONAL REFERENCES

117. Berg, S., Kutra, D., Kroeger, T., Straehle, C.N., Kausler, B.X., Haubold, C., Schiegg, M., Ales, J., Beier, T., Rudy, M., et al. (2019). ilastik: interactive machine learning for (bio)image analysis. Nat Methods *16*, 1226–1232. https://doi.org/10.1038/s41592-019-0582-9.

118. Ma, J., He, Y., Li, F., Han, L., You, C., and Wang, B. (2024). Segment anything in medical images. Nat Commun *15*, 654. https://doi.org/10.1038/s41467-024-44824-z.

119. Klein, S., Staring, M., Murphy, K., Viergever, M.A., and Pluim, J. (2010). elastix: A Toolbox for Intensity-Based Medical Image Registration. IEEE Trans. Med. Imaging *29*, 196–205. https://doi.org/10.1109/TMI.2009.2035616.

120. Wang, F., Flanagan, J., Su, N., Wang, L.-C., Bui, S., Nielson, A., Wu, X., Vo, H.-T., Ma, X.-J., and Luo, Y. (2012). RNAscope: A Novel in Situ RNA Analysis Platform for Formalin-Fixed, Paraffin-Embedded Tissues. The Journal of Molecular Diagnostics *14*, 22–29. https://doi.org/10.1016/j.jmoldx.2011.08.002.

ACKNOWLEDGEMENTS

We thank members of the Luo Lab, especially Ellen Gingrich, Tom Hindmarsh-Sten, Lijun Qi, Zhuoran Li, Alex Starr, Yunming Wu, and Cheng Lyu, as well as Julia Kaltschmidt, Jennifer Raymond, and Kang Shen for their support, expertise, and insights on this study. We also thank Caiying Guo and the Transgenic Facility at Janelia Research Campus for the cTAG mice; Yiming Zhang, Huyan Meng, and Zhigang He at the Boston Children's Hospital Viral Core for the *LV-FlpO-GFP* virus; Artur Kania and Kevin Sangster for feedback on the manuscript; Kenneth Magpusao and Carlota Manalac for animal assistance; David Luginbuhl and Mary Molacavage for administrative assistance. D.T.P. was supported by the American Australian Association Education Fund Scholarship. L.L. is an HHMI investigator. This work was supported by the National Institutes of Health (R01-NS050580 to L.L.), and the Simons Foundation (SFARI Fellows-to-Faculty Award to D.T.P.)

AUTHOR CONTRIBUTION

L.L., D.T.P., and U.C. conceived the project and designed all experiments. U.C. and D.T.P. performed majority of the experiments and data analyses. J.H.S. performed whole brain registration and Dice coefficient analyses, and Y.Z. conducted the *in situ* hybridization assays. I.R. assisted with the iDISCO experiments. L.L. and D.T.P. supervised the study. U.C., D.T.P., and L.L. wrote the manuscript.

DECLARATION OF INTERESTS

The authors declare that they have no competing interests.

RESOURCE AVAILBILITY

Materials Availability

Plasmids generated for the *LV-FlpO-GFP* virus will be deposited. Mouse lines generated in this study will be deposited to the Jackson Laboratory.

Data and Code Availability

Source data are provided in the manuscript. Interactive platform (Supplementary Data 1) and raw images of whole brain staining of Ten3 and Lphn2 across development will be deposited. Code will be available on Github. All access will be released upon publication.

SUPPLEMENTARY MATERIALS

Supplementary Data 1 | Interactive visualization of Ten3 and Lphn2 expression in horizonal sections of E17 and P2 mouse brains

Video S1 | Three-dimensional reconstruction of whole brain Ten3 and Lphn2 expression across developmental stages

Video S2 | Horizontal section series showing whole brain Ten3 and Lphn2 expression at postnatal day 0

Video S3 | Three-dimensional reconstruction of the caudate putamen and external segment of the globus pallidus

Video S4 | Three-dimensional reconstruction of Ten3 and Lphn2 expression in the cerebellar cortex
Video S5 | Three-dimensional reconstruction of Ten3 and Lphn2 expression in the cerebellar nuclei
Video S6 | Three-dimensional reconstruction of zebrin expression in the cerebellar cortex